Effect of Nozzle Port Angle on Transient Flow and Surface Slag Behavior During Continuous Steel-Slab Casting

SEONG-MOOK CHO, BRIAN G. THOMAS, and SEON-HYO KIM

Undesirable flow variations can cause severe instabilities at the interface between liquid mold flux and molten steel across the mold top-region during continuous steel casting, resulting in surface defects in the final products. A three-dimensional Large Eddy Simulation (LES) model using the volume of fluid method for the slag and molten steel phases is validated with plant measurements, and applied to gain new insights into the effects of nozzle port angle on transient flow, top slag/steel interface movement, and slag behavior during continuous slab casting under nominally steady conditions. Upward-angled ports produce a single-roll flow pattern with lower surface velocity, due to rapid momentum dissipation of the spreading jet. However, strong jet wobbling from the port leads to greater interface variations. Severe level drops allow easy entrapment of liquid flux by the solidifying steel shell at the meniscus. Sudden level rises may also be detrimental, leading to overflow of the solidified meniscus region. Downward-angled ports produce a classic double-roll pattern with less jet turbulence and a more stable interface everywhere except near the narrow faces. Finally, the flow patterns, surface velocity, and level predicted from the validated LES model are compared with steady-state standard k-ε model predictions.

I. INTRODUCTION

MANY defects in final steel products manufactured from continuous casting processes are caused by unoptimized surface flow, including excessive or insufficient surface velocity, vortex formation, and severe surface level fluctuations in the mold. These undesirable phenomena can produce slag defects by several mechanisms.[1] High surface velocity, above the optimum range,[2] may lead to surface instability and slag entrainment.[3,4] On the other hand, insufficient surface flow may cause problems during initial steel solidification such as deep oscillation marks,[5] hook formation,[6] and insufficient slag infiltration, leading to high or nonuniform meniscus heat transfer and surface cracks. Vortex formation, such as caused by asymmetric surface flow, can entrain slag from the mold top surface by pulling funnels of slag down into the molten steel pool.[7–9] These mechanisms are usually associated with abnormal behavior, such as nozzle clogging[10] or stopper-rod misalignment,[11] and typically lead to internal, subsurface defects when the slag droplets are entrapped into the solidifying shell below the meniscus. However, surface level fluctuations near the meniscus on the Wide Faces (WFs) and Narrow Faces (NFs) can push the slag down beneath the solidifying steel shell, to become entrapped near the meniscus, leading to surface defects.[12,13] Sudden level rises may overflow the meniscus, leading to internal scale and slag entrapment, especially if meniscus solidification and hook formation is significant. Level fluctuations depend on transient flow in the nozzle and mold, and is related to swirl flow variations inside the nozzle, leading to jet wobbling in the mold cavity, and surface velocity variations even during nominally steady-state casting conditions.[14]

Previous work has suggested that single-roll flow patterns are more detrimental than double roll,[15,16] although the detailed mechanisms are somewhat unclear and unquantified. Many works have investigated the effect of different casting parameters on fluid flow in the nozzle and mold, including casting speed, submergence depth of the nozzle,[17] argon gas injection,[15,16,18–20] electro-magnetic fields,[14,17,21–23] and nozzle geometry

SEONG-MOOK CHO is with the with the Department of Mechanical Engineering, Colorado School of Mines, 1610 Illinois Street, Golden, CO 80401. BRIAN G. THOMAS is with the Department of Mechanical Engineering, Colorado School of Mines and also with the University of Illinois at Urbana-Champaign, 1206 West Green Street, Urbana, IL 61801. Contact e-mail: bgthomas@mines.edu SEON-HYO KIM is with the Department of Materials Science and Engineering, Pohang University of Science and Technology, 77 Cheongam-Ro, Nam-Gu, Pohang, Gyeongbuk 790-784, Republic of Korea.

including slide-gate orientation,[18] port angle,[24–26] port size,[25] port shape,[25,27,28] and bottom design.[25,29,30] Nozzle geometry directly influences the mold flow pattern by changing the jet flow characteristics exiting the ports. Najjar *et al.* investigated the effect of several nozzle design parameters on the jet characteristics and found that jet angle is controlled mainly by the port angle.[25] Upward-angled ports produce stronger jet wobbling resulting in higher surface velocity fluctuations, compared to downward-angled ports.[26] Relative to a mountain-shaped nozzle bottom, a nozzle with a well-bottom leads to lower surface velocity and turbulence, and with less surface level fluctuations.[29] Salazar-Campoy et. al. claimed that adding a groove to the port bottom led to smaller bubble sizes and less turbulent flow.[28] Most of these previous studies have focused on time averages from water model experiments or/and computational models. However, most defects are related to transient flow phenomena, and details of the formation mechanisms have not been quantified.

In this work, multiphase flow simulations using a three-dimensional Large Eddy Simulation (LES) model coupled with a volume of fluid (VOF) model to capture the slag and molten steel phases are applied to quantify transient fluid flow and behavior of the liquid mold flux/molten steel interface in continuous steel-slab casting. The domain includes the tundish-bottom, stopper-rod, nozzle, mold, and upper-strand regions. Simulations are conducted for two different nozzle geometries with different port angles (upward and downward) with other casting conditions maintained constant, as given in Table I. Surface velocities in the mold are measured by performing nail dipping tests in a commercial stainless-steel caster, and meniscus profiles are captured by tracing the oscillation marks on the steel-slab surface, and used to validate the LES model predictions. Finally, the validated LES model is compared with a Reynolds-Averaged Navier-Stokes (RANS) model using the standard k-ε model to predict mold flow pattern, turbulence, surface velocity, and surface level.

II. COMPUTATIONAL MODELS

A transient three-dimensional finite-volume LES model, coupled with a VOF model, has been developed to calculate molten steel flow field and liquid mold flux/molten steel interface behavior in the mold region of a typical continuous steel-slab caster.

A. *Governing Equations*

Mass conservation of the molten steel and the liquid mold flux phases together are satisfied using a single continuity equation:

$$\frac{\partial \rho_{\mathrm{mix}}}{\partial t} + \nabla \cdot (\rho_{\mathrm{mix}} \boldsymbol{u}) = S_{\mathrm{shell,mass}}, \qquad [1]$$

where $\boldsymbol{u}$ is the vector of velocity components of the mixture of molten steel and liquid mold flux, $S_{\mathrm{shell,mass}}$ is a mass sink term applied to cells next to the domain

boundaries representing the steel shell to account for flow across the solidification front.[31–33] In the current model, mass sink of the mold flux is not considered because there is no slag consumption or solidification in the domain. These phenomena occur mainly outside of the domain. Thus, the inflow of slag due to melting at the top domain wall representing the interface between liquid and sintered slag is assumed to exactly balance the rate of consumption, so both are set to zero. ρ_{mix} is mixture density, based on the phase volume fractions, as follows:

$$\rho_{\mathrm{mix}} = \alpha_{\mathrm{s}} \rho_{\mathrm{s}} + \alpha_{\mathrm{f}} \rho_{\mathrm{f}}, \qquad [2]$$

where α_{s} is volume fraction of molten steel, α_{f} is volume fraction of liquid mold flux, ρ_{s} is density of the molten steel, and ρ_{f} is density of the liquid mold flux given in Table II.

The volume fraction of liquid mold flux, α_{f} is tracked with the following VOF equation:

$$\frac{\partial(\alpha_{\mathrm{f}}\rho_{\mathrm{f}})}{\partial t} + \nabla \cdot (\alpha_{\mathrm{f}}\rho_{\mathrm{f}}\boldsymbol{u}) = 0 \qquad [3]$$

and the volume fraction of molten steel, α_{s} is found from $\alpha_{\mathrm{s}} = 1 - \alpha_{\mathrm{f}}$.

A single set of time-dependent momentum balance equations is solved for the two-phase mixture of molten steel and liquid mold flux, considering the movement of the solidifying steel shell and interfacial surface tension,

$$\begin{aligned} \frac{\partial(\rho_{\mathrm{mix}}\boldsymbol{u})}{\partial t} + \nabla \cdot (\rho_{\mathrm{mix}}\boldsymbol{u}\boldsymbol{u}) = & -\nabla p + \nabla \\ & \cdot \left[(\mu_{\mathrm{mix}} + \mu_{\mathrm{t}}) (\nabla \boldsymbol{u} + \nabla \boldsymbol{u}^T) \right] \\ & + \rho_{\mathrm{mix}} \boldsymbol{g} + \boldsymbol{S}_{\mathrm{shell,mom}} \\ & + \boldsymbol{F}_{\mathrm{interface}}, \end{aligned}$$
$$[4]$$

where μ_{mix} is mixture dynamic viscosity ($\mu_{\mathrm{mix}} = \alpha_{\mathrm{s}}\mu_{\mathrm{s}} + \alpha_{\mathrm{f}}\mu_{\mathrm{f}}$), μ_{s} and μ_{f} are dynamic viscosities of the molten steel and the liquid mold flux, respectively, given in Table II, μ_{t} is turbulent viscosity modeled with the Wall-Adapting Local Eddy (WALE) sub-grid-scale viscosity model,[34,35] to account for turbulent eddies too small to be resolved by the mesh, g is gravity acceleration, $S_{\mathrm{shell,mom}}$ is a momentum sink term, applied in each component direction to account for solidification, similar to $S_{\mathrm{shell,mass}}$,[31–33] and $\boldsymbol{F}_{\mathrm{interface}}$ is interfacial tension between the two phases, calculated by the Continuum Surface Force model as follows:

$$\boldsymbol{F}_{\mathrm{interface}} = \sigma_{s-f} \frac{\rho_{\mathrm{mix}} \kappa \nabla \alpha_f}{\frac{1}{2}(\rho_s + \rho_f)}, \qquad [5]$$

where $\sigma_{\mathrm{s\text{-}f}}$ is the surface tension coefficient for liquid mold flux/molten steel interface calculated using Eq. [6], and κ is the local curvature of liquid mold flux/molten steel interface.

$$\sigma_{s-f} = \frac{\sigma_{s-ss} - \sigma_{f-ss}}{cos\theta}, \qquad [6]$$

Table I. Caster Dimensions and Process Conditions

Caster dimensions
  Nozzle bore inner diameter D_{in}: 65 mm (at UTN top) to 60 mm (at bottom well)
  Nozzle bore outer diameter D_{out}: 110 mm
  Nozzle bottom well depth d: 11 mm
  Nozzle port width   60 mm
  Nozzle port height   Case 1: h: 65 mm, h': 67.3 mm
       Case 2: h: 65 mm, h': 75.1 mm
  Nozzle port angle (both top and bottom edges)   Case 1: θ: + 15 deg (up)
       Case 2: θ: − 30 deg (down)
  Nozzle length   1250 mm
  Area ratio between two ports and nozzle bore   2.54
  Mold thickness   200 mm
  Mold width   1600 mm
  Domain length   4780 mm (total); 2790 mm (mold and strand regions)
Process conditions
  Steel flow rate   256 LPM (1.8 tonne/min)
  Casting speed   0.8 m/min (13.3 mm/s)
  Submerged depth of nozzle   140 mm
  Meniscus level below mold top   100 mm
  Average thickness of liquid mold flux layer on molten steel pool L_{lm}: 10 mm

Table II. Fluid Properties

Material	Density (kg/m^3)	Dynamic viscosity (kg/m·s)
Molten stainless steel	7200	0.006
Liquid mold flux	3000	0.18

Table III. Interfacial Tension and Contact Angle at Liquid Mold Flux/Molten Steel/Steel Shell Interface

Parameter	Value
Interfacial tension between molten steel and liquid mold flux: σ_{s-f}	1.3 N/m
Interfacial tension between molten steel and solid steel shell[36–40]: σ_{s-ss}	1.6 N/m
Interfacial tension between liquid mold flux and solid steel shell[5,41]: σ_{f-ss}	0.42 N/m
Contact angle on liquid mold flux/molten steel/steel shell[12]: θ	20 deg

where σ_{s-ss}[36–40] and σ_{f-ss}[5,41] are surface tension coefficients, respectively, for the molten steel/solid steel shell interface and the liquid mold flux/solid steel shell interface, and θ is contact angle at the 3-phase boundary between the liquid mold flux, molten steel, and solid steel shell.[12] The values of these parameters are given in Table III.

To quantify the fluctuations of each velocity component from the LES-VOF simulations, the Root Mean Square (RMS) of the velocity fluctuations for each component, $\sqrt{\overline{(u_i')^2}}$ are calculated as follows:

$$\sqrt{\overline{(u_i')^2}} = \sqrt{\frac{1}{n}\sum_{t=0}^{n}\left(u_{i,t} - \overline{u_{i,t}}\right)^2}, \qquad [7]$$

where i is the coordinate (x, y, and z), t is time step, and n is the total number of time steps in the time-averaging period.

From the RMS of the velocity fluctuations, Turbulent Kinetic Energy (TKE) is calculated as follows:

$$\text{TKE} = \frac{\left[\sqrt{\overline{(u_x')^2}}\right]^2 + \left[\sqrt{\overline{(u_y')^2}}\right]^2 + \left[\sqrt{\overline{(u_z')^2}}\right]^2}{2}. \qquad [8]$$

To understand liquid mold flux/molten steel interface instability, the time average of the interface level fluctuations, σ_x is calculated as follows:

$$\sigma_x = \sqrt{\frac{1}{n}\sum_{t=0}^{n}(x_t - \overline{x_t})^2}, \qquad [9]$$

where x_t is the instantaneous liquid mold flux/molten steel interface level, and $\overline{x_t}$ is the mean level at that location.

B. Domain, Mesh, and Boundary Conditions

The LES coupled with VOF model adopts the full domain of a real caster, including part of the tundish bottom, the stopper-rod region, the Upper Tundish

Nozzle (UTN), Submerged Entry Nozzle (SEN) with nozzle ports, the top 3000 mm of the molten steel pool in the mold and strand, and a 10-mm-thick layer of liquid mold flux layer at the mold top surface. In order to achieve accurate flow calculations in the stopper region and below, the domain was extended upstream to include a cylindrical region of the tundish bottom around the stopper. The domain is meshed with over 4 million hexahedral cells: Case 1 with + 15 deg (upward) ports and Case 2 with − 30 deg (downward) ports, including 1mm cell length across the liquid mold flux layer and molten steel pool region near the interface between two phases. The schematic of domain and mesh for the LES simulations are shown in Figure 1. The steel shell-thickness profile down this caster is shown in Figure 2 and is given by

$$S \text{ (mm)} = k_c \sqrt{t(\text{sec})}, \qquad [10]$$

where S is steel shell thickness at location below meniscus, t is time for steel shell to travel to the location, and constant k_c was estimated to be $3.37 \text{ mm/sec}^{1/2}$ based on shell-thickness measurements of a breakout shell.

Constant velocity was fixed as the inlet condition at the outside surface of a cylinder of fluid near the tundish bottom. This velocity (0.0014 m/s) was calculated according to the molten steel flow rate and the surface area (0.982 m^2) of the cylindrical region. A pressure outlet condition was chosen on the domain bottom at the mold exit as 117 kPa gauge pressure considering the ferrostatic pressure due to the head of molten steel. The interface at the top surface wall (interface between the liquid mold flux and the sintered mold flux) was given a no-slip condition, which reflects that the sintered mold flux has much higher dynamic viscosity.[42–44] The domain wall representing the interface between the molten steel fluid and the solid steel shell was given by a no-slip wall moving downward at the casting speed.
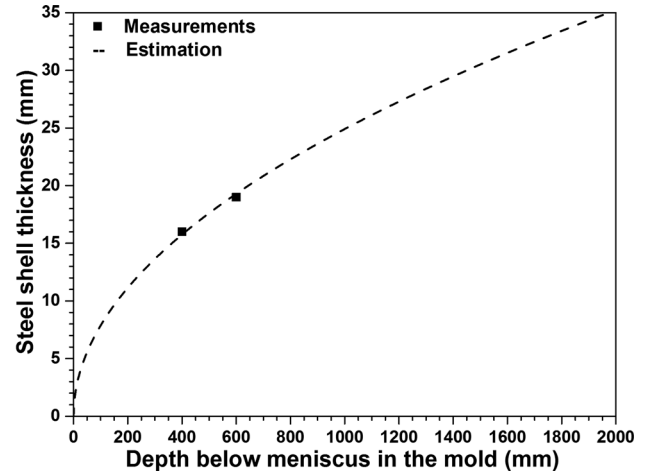

Fig. 2—Solidifying steel shell-thickness profile down the strand and model domain.
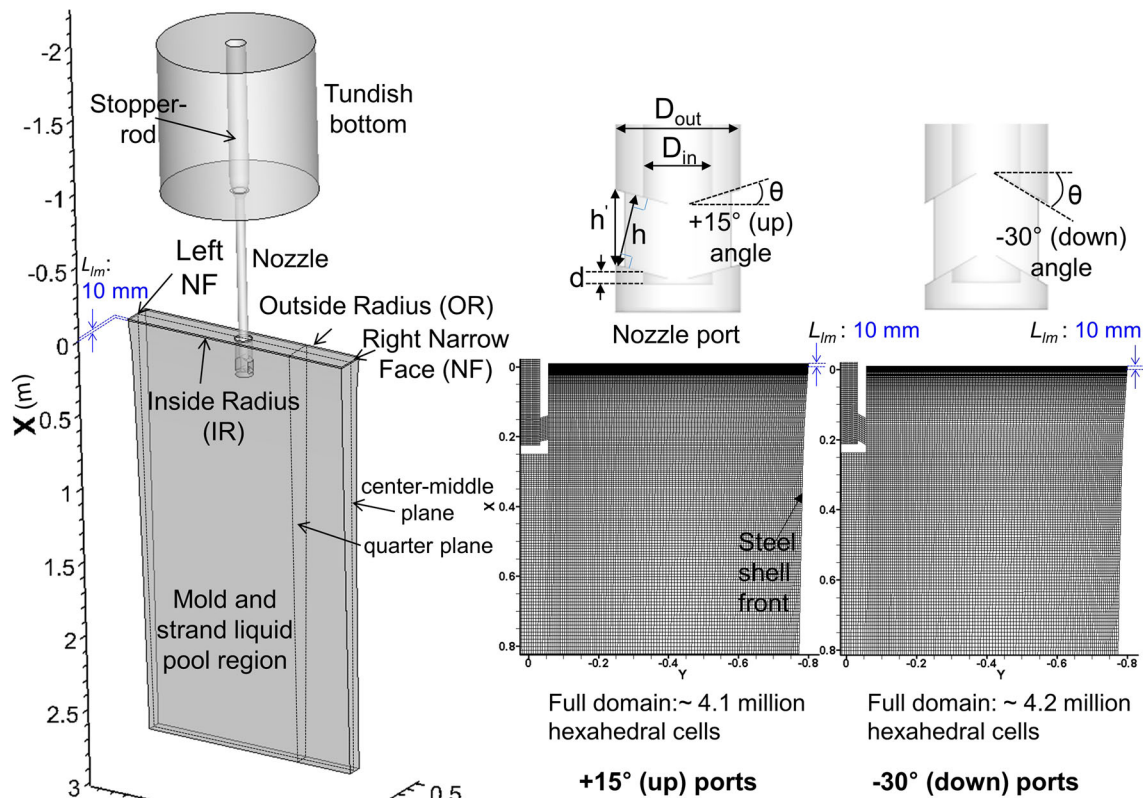

Fig. 1—Domain and mesh of the computational models.

C. *Numerical Details*

The five equations for the three momentum components, pressure implemented with the pressure Poison equation, and interface motion with VOF were discretized using the finite-volume method in ANSYS FLUENT.[34] The mass and momentum sink terms, $S_{shell,mass}$ and $\boldsymbol{S}_{shell,mom}$, are implemented with User Defined Functions.[31–33] These discretized equations were solved for velocity and pressure by the Semi-Implicit Pressure Linked Equations (SIMPLE) algorithm, initiating from zero velocity in all cells. To better resolve the transient interface between liquid mold flux and molten steel, a second-order reconstruction (compressive) scheme for the volume fraction field was used for the VOF model. Starting at time = 0 seconds, the LES model was run for ~ 55 seconds using a constant time step of 0.001 seconds. The flow was allowed to develop for ~ 17 seconds, and then a further ~ 38 seconds of data was used to compile time averages, of which ~ 18 seconds was used to compile standard deviations for level fluctuations.

III. PLANT MEASUREMENTS

A. *Nail Dipping Tests*

Nail dipping tests were conducted to quantify surface velocity and flow direction near the mold top surface during steady continuous casting. Several pairs of 5-mm-diameter, 290-mm-long stainless-steel nails, spaced 100 mm apart, were dipped for 3 seconds at 2-minute intervals, at 200 mm from the narrow face. The solidified lump on each nail was measured for lump diameter, φ_{lump} (mm) and lump height difference, h_{lump} (mm), as shown in Figure 3, and used to estimate velocity magnitude according to[45]

$$U_{surface} = 0.624 \left(\varphi_{lump}\right)^{-0.696} \left(h_{lump}\right)^{0.567}. \quad [11]$$

From the resulting histories of velocity magnitude and flow direction, the time average and variations of each velocity component were evaluated to validate the model predictions.

B. *Oscillation-Mark Profile Measurements*

Oscillation marks are small transverse depressions in outer surfaces of solidifying steel shells, produced by freezing and partial overflow of the molten steel over the meniscus during each mold oscillation cycle. Thus, each mark captures the instantaneous shape of the interface between the liquid mold flux and molten steel around the mold perimeter. In this work, the narrow face of the slab sample, including ten oscillation marks, was sand blasted to reveal the surface, as shown in Figure 4. The oscillation-mark lines were traced and graphed, maintaining total area under each curve of zero. These lines reveal variations of the liquid mold flux/molten steel interface profiles, that were used to validate the LES-VOF model predictions.
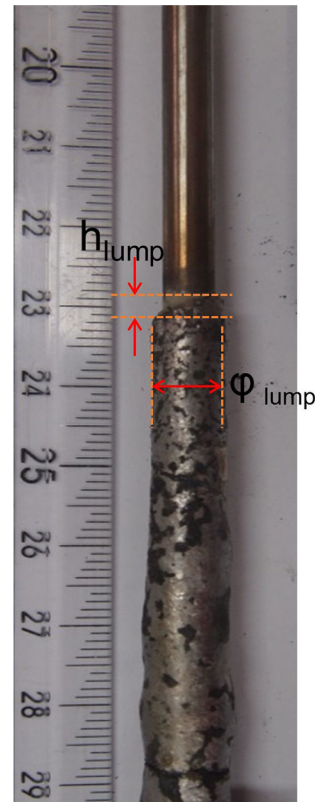

Fig. 3—Example solidified lump from nail dipping tests.

IV. NOZZLE FLOW

To investigate the effect of port angle on fluid flow in the nozzle, the coupled LES-VOF model was used to calculate transient fluid flow in the nozzle and mold during nominally steady slab casting with two different port angles: upward (Case 1: + 15 deg (up) angle) and downward (Case 2: − 30 deg (down) angle). Time-averaged and transient flow patterns, and Turbulent Kinetic Energy (TKE) are quantified at the center-middle plane (between Inside Radius (IR) and Outside Radius (OR) shell surfaces of the strand wide faces), and at the port outlets of the nozzle in Figures 5 and 6. In addition, mean jet flow characteristics, including velocity components, mean jet speed, vertical and horizontal jet angles and spread angles, Root Mean Square (RMS) of velocity fluctuations, and turbulent kinetic energy, were calculated in the port outlet planes using weighted-average relations based on positive outward flow,[25,46] (which ignore backflow regions), and are given in Table IV. Appendix explains the spread angle equations.

The upward-ports case produces a vertical jet angle of + 6.51 deg (up: toward mold top surface) with a vertical spread angle of 11.5 deg. Jet flow from the downward-ports case is steeper with an angle of − 30.6 deg (downward) into the mold bottom and has a slightly larger vertical spread angle (16.2 deg). In both cases, the jet is angled steeper downward than the nozzle port angle, which agrees with previous work.[25,26] This behavior is because the over-sized nozzle ports (large

Fig. 4—Ocillation mark profiles on the steel slab: narrow face view.

Time averaged 37.5 sec (16.8 to 54.3 sec)

+15° (up) ports

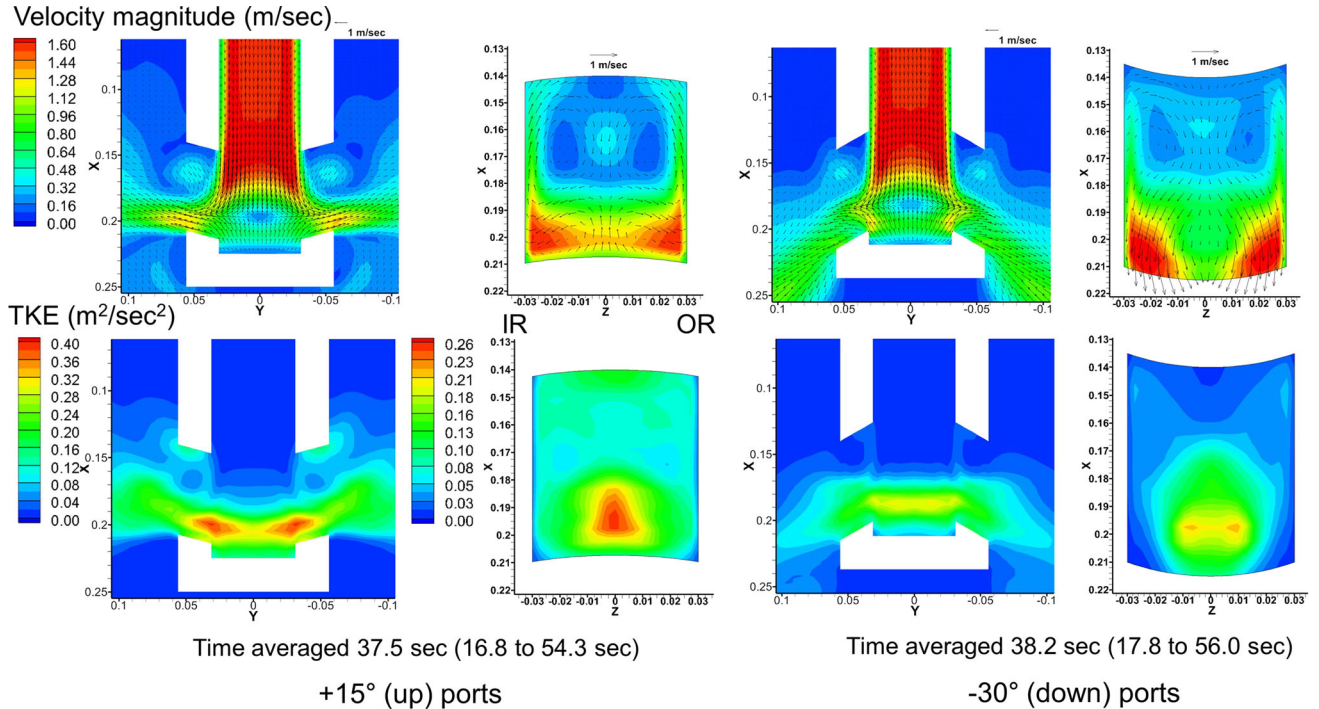Time averaged 38.2 sec (17.8 to 56.0 sec)

-30° (down) ports

Fig. 5—Time-averaged flow pattern and turbulent kinetic energy at the center-middle plane (between IR and OR) and the nozzle port outlet for upward and downward port angles: LES-VOF model.

area ratio, 2.5, of the nozzle ports to nozzle bore), and relatively thin nozzle walls, (see Table I) together enable the jet to maintain some of its downward momentum.[25,26] Just after leaving the ports, the jet angles become even steeper downward, as shown in Figure 5. Both port angles produce ~ 0 deg horizontal jet angle, which indicates symmetry between IR and OR. Considering that the model geometries and conditions are symmetrical, this finding indicates that 38 seconds of flow time simulated (for time average) is sufficient to capture the transient variations. The jet from the upward-angled nozzle port has more horizontal spread (3.38 deg) than the downward-ports jet (1.21 deg).

Transient flow in the nozzle bottom region produces asymmetrical counter-rotating double swirling patterns at the port outlet, showing both clockwise and counter-clockwise flow with both port angles. With the upward ports, the swirl flow is stronger and asymmetry between the two swirls is more severe. As shown in Figure 6, the larger swirl occupies ~ 2/3 of the port area, and alternates with time between left (IR) and right (OR) being larger. This contrasts with the single swirl patterns usually observed in slide-gate nozzles, which are stronger and take up the entire port area.[14,47] With the more symmetrical stopper-rod flow, two swirls always occur. The stronger and more asymmetrical swirling in the nozzle with the upward ports makes the jet flow more unstable. On the other hand, the downward ports produce smooth and stable jet flow. Thus, the velocity fluctuations (RMS of each velocity component) are all much higher with the upward ports, as given in Table IV. This results in twice as large TKE of the jet flow at the nozzle port with the upward angle, as shown in Figure 5. The severe interruption of the
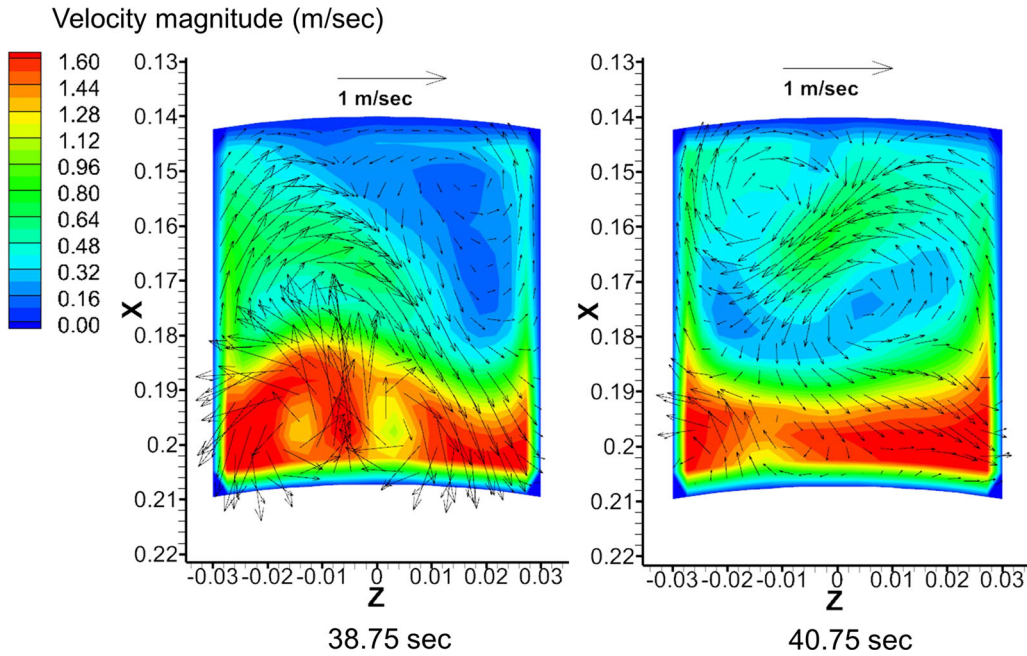
Fig. 6—Two instantaneous flow patterns exiting the nozzle port with upward angle.

Table IV.   Mean Jet Flow Characteristics at Nozzle Port (from LES model)

	Case 1. + 15 deg (Up)	Case 2. − 30 deg (Down)
Weighted-average x velocity (downward): $\bar{u}_x$	− 0.12 m/s	0.52 m/s
Weighted-average y velocity (horizontal toward NF): $\bar{u}_y$	1.07 m/s	0.89 m/s
Weighted-average z velocity (horizontal toward OR WF): $\bar{u}_z$	− 0.000056 m/s	− 0.00017 m/s
Weighted-average RMS of x velocity fluctuations: $\sqrt{\overline{(u'_x)}^2}$	0.31 m/s	0.21 m/s
Weighted-average RMS of y velocity fluctuations: $\sqrt{\overline{(u'_y)}^2}$	0.27 m/s	0.23 m/s
Weighted-average RMS of z velocity fluctuations: $\sqrt{\overline{(u'_z)}^2}$	0.21 m/s	0.12 m/s
Average jet speed: $\overline{U}$	1.08 m/s	1.03 m/s
Maximum velocity magnitude: $u_{\text{Max,mag}}$	1.74 m/s	1.83 m/s
Vertical jet angle (positive toward surface): θ_{xy}	+ 6.5 deg	− 30.6 deg
Horizontal jet angle (positive toward OR): θ_{yz}	− 0.003 deg	− 0.011 deg
Vertical spread angle: $\theta_{xy,sp}$	11.5 deg	16.2 deg
Horizontal spread angle (toward WFs): $\theta_{yz,sp}$	6.8 deg	2.4 deg
Weighted-average turbulent kinetic energy: k	0.106 m^2/s^2	0.056 m^2/s^2
Back flow zone	19.0 pct	19.9 pct

downward flow by the upward ports is nonuniform, resulting in severe turbulent fluctuations at the port region. This trend matches previous results.[24–26]

V.   MOLD FLOW

Flow in the mold, including jet flow, surface flow, slag entrainment, liquid mold flux/molten steel interface motion, slag entrapment during level drops, and flow near the meniscus, is quantified in this section for both upward- and downward-ports cases. In addition, the predicted surface velocities, interface profiles, and their fluctuations are compared with plant measurements from nail dipping tests and oscillation-mark visualization to validate the LES-VOF model.

A. Jet Flow

Jet flows into the mold generate very different flow patterns with the two different port angles, as shown in Figure 7. The upward-ports case produces a single-roll flow pattern, as the high-spreading jet impinges first onto the wide faces, and deflects upward to impinge into the mold top surface, midway between the SEN and the NF. The downward-ports case generates a classic

double-roll flow pattern, where the less-spreading jet impinges first onto the narrow face, and splits to send flow up the narrow face toward the top surface. Cross sections through both jets, given in Figure 8 at the quarter plane (midway between SEN and right NF), confirm the tight circular-shaped jet from the downward ports.

Time variations of the velocity components of the jet flows from both nozzles are shown in Figure 9. Both jets exhibit wobbling behavior, which is visualized by the animations in Supplementary Materials 1 and 2. In particular, the upward ports produce severe up-and-down variations (in the casting direction) compared with the downward ports (Table V). This leads to more time variation of the impingement location for the upward ports. These velocity variations in the y–z direction on the top surface are $\sim 2.2 \times$ greater than those for the downward ports. This corresponds to higher TKE of the jet in the mold with the upward ports, in addition to higher TKE at the surface, compared with the stable double-roll flow pattern with the downward ports, as shown in Figure 7.

B. Surface Flow

Jet flow from the upward ports impinging on the top surface leads to slightly slower time-averaged surface flow, compared with the downward ports, as shown in Figure 10. This is because the jet momentum from the upward ports is diffused by the broader, wider jet, which lowers its velocity. On the other hand, surface flow toward the SEN with the downward ports is slightly faster, and more uniform across the mold surface.

Figure 11 shows time-averaged and instantaneous surface velocities measured using the nail dipping tests 200 mm from the right narrow face (600 mm from the mold center), with the upward ports. The transient surface flows in both IR and OR regions 50 mm from the wide faces during the 8-minute period are visualized 2 minutes apart by scaled arrows showing both flow direction and velocity magnitude. During the 8 minutes, the flow at these locations is very chaotic, as the flow pattern varies from strong flow toward the narrow face to strong rotation in both clockwise and

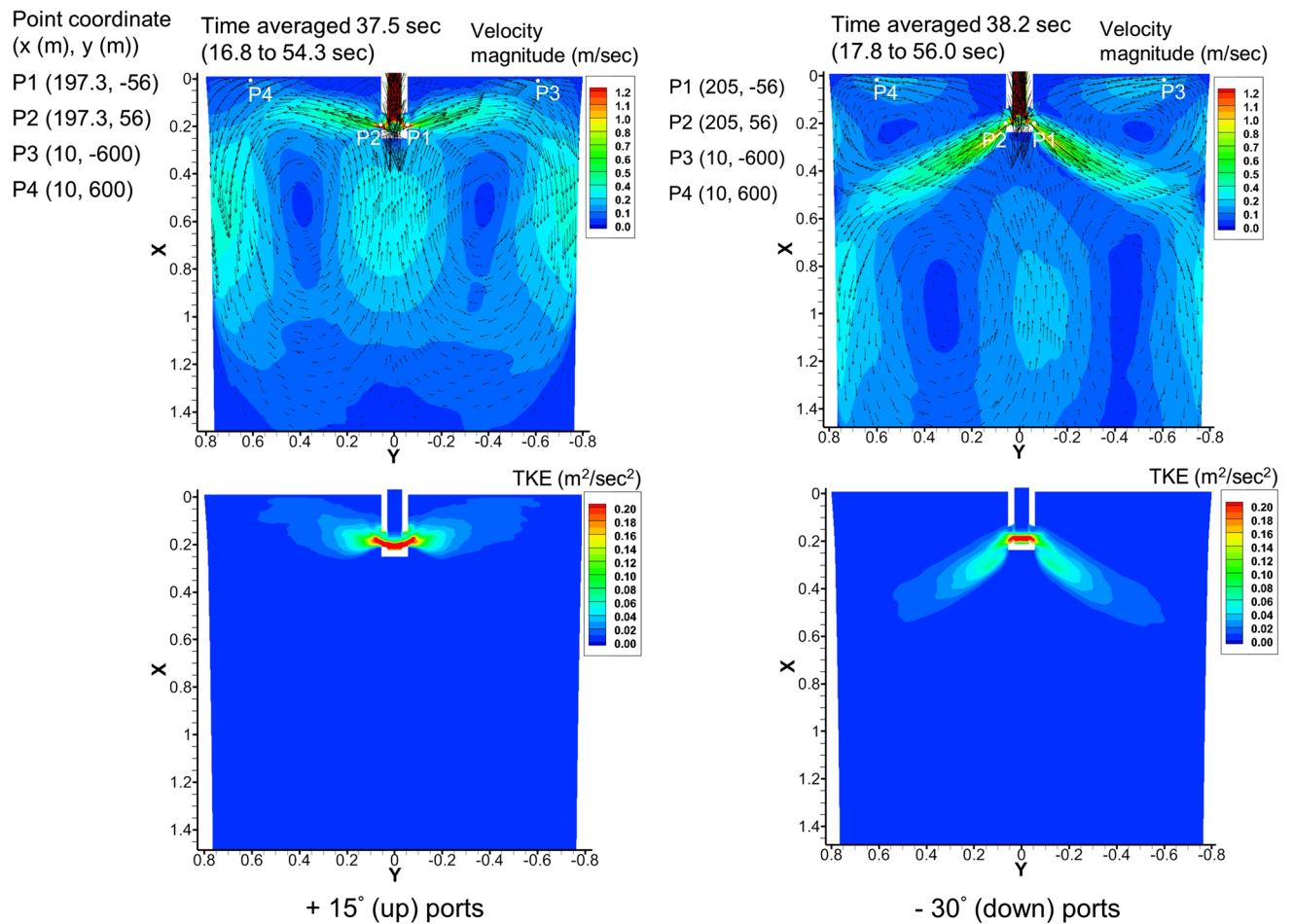+ 15° (up) ports   - 30° (down) ports

Fig. 7—Time-averaged flow pattern and turbulent kinetic energy at the center-middle plane in the mold with upward- and downward-angled ports.
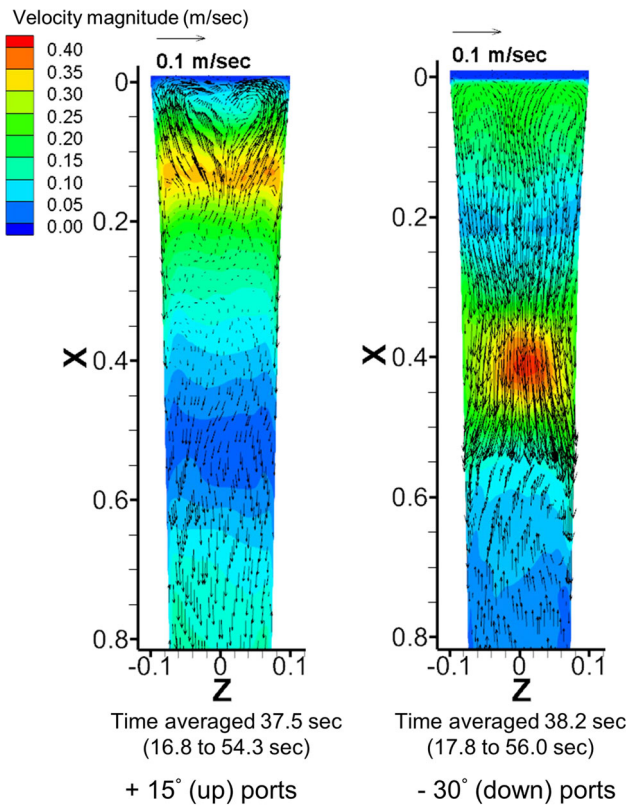
Fig. 8—Time-averaged jet flow patterns at the quarter plane (between SEN and right NF: 400 mm from mold center) in the mold with upward- and downward-angled ports.

counter-clockwise directions. This suggests that strong level fluctuations and defects are very likely associated with this flow behavior.

As shown in Figure 11, the time average of the measurements suggests that the wide jet splits into two flows, which rise up the IR and OR and impinge into each other after meeting at the top surface. The same behavior is observed in the model simulation velocities in Figure 8. Simulated histories of the surface velocity at the measured location (at both symmetrical points P3 and P4) are compared for both cases in Figure 12. In addition to matching the measured trends, the predictions generally fall within the quantitative range of the measurements, and the time means agree reasonably as well.

Even though average surface velocity in the mold with the upward ports is almost half of the surface velocity with the downward ports, the surface velocity fluctuations are much more severe with the upward ports. With the upward ports, severe velocity fluctuations occur, which are much larger than those with the downward ports: ~1.8× greater across the mold width (y direction) and ~ 1.5 × greater cross the mold thickness (z direction), as shown in Table VI. This causes ~ 2 × larger TKE at the surface with the upward nozzle as shown in Figure 10. Thus, the surface flow with the upward ports produces more instabilities at the interface between the liquid mold flux and the molten steel (see Supplementary

Animations 3 and 4). Figure 13 shows the power of both the y and z velocity components at P3. They are higher at the mold surface with the upward ports. It is important to note that the z velocity component, which is related to fluctuations of the cross-flow between wide faces in the mold, shows a huge power peak at ~ 0.12 Hz with the upward ports. This reveals that the strongest velocity fluctuations at the mold surface occur periodically, every ~ 8.3 seconds.

C. Slag Entrainment

Turbulent steel flow at the slag-steel interface may push or drag the liquid mold flux *via* shear, leading to the entrainment of slag droplets into the flowing steel. The flow also may cause sudden level fluctuations, leading to slag entrapment into the solidifying steel shell, if the fluctuations occur near the meniscus. Other entrained slag droplets in the molten steel pool may become entrapped into the solidifying steel shell, after they are transported through the turbulent flowing steel, contact the shell, and satisfy the capture criterion. The remaining entrained droplets are absorbed safely back into the slag layer. Increased surface velocity increases the possibility of slag entrainment *via* the upward flow mechanism,[48] and shear layer instability.[49–51] Figure 14 shows time variations of surface velocity magnitude (at P3 and P4) with critical surface velocities based on these slag entrainment mechanisms for both the upward and downward ports. Average velocity magnitude with the downward ports is higher than the upward ports. However, the results showing mean velocity are less than the thresholds for slag entrainments, so chronic entrainment problems are not expected from either nozzle.

Figure 15 shows instantaneous liquid mold flux behavior and flow velocity in the mold for both upward and downward ports from Supplementary Materials 3 and 4. With the upward ports, a finger-like protrusion from the liquid mold flux layer was observed where the jet impinges and many large, low-slag-fraction (~ 0.05 volume fraction) regions are observed in the molten steel pool in Figure 15(a)). The cell volumes near the slag/molten steel interface are too big, (8 mm across mold width, 4 mm across mold thickness, and 1 mm across slag/molten steel interface) to resolve small slag droplets. These entrained regions with low-slag fraction can be converted into an estimated equivalent diameter of pure slag droplets, d_f as follows:

$$d_f = \sqrt[3]{\frac{6}{\pi} \alpha_f V_{cell}}, \qquad [12]$$

where α_f is volume fraction of slag in the cell and V_{cell} is cell volume. Slag droplet diameters of ~1 mm are estimated. Thus, the true physics of the slag entrainment mechanism cannot be fully captured. However, numerical diffusion is greater for conditions leading to slag entrainment (*e.g.*, high velocity and shear across the interface) as well as for level drops (accompanying entrapped slag at the meniscus), level fluctuations, and velocity variations in the bulk (potentially leading to
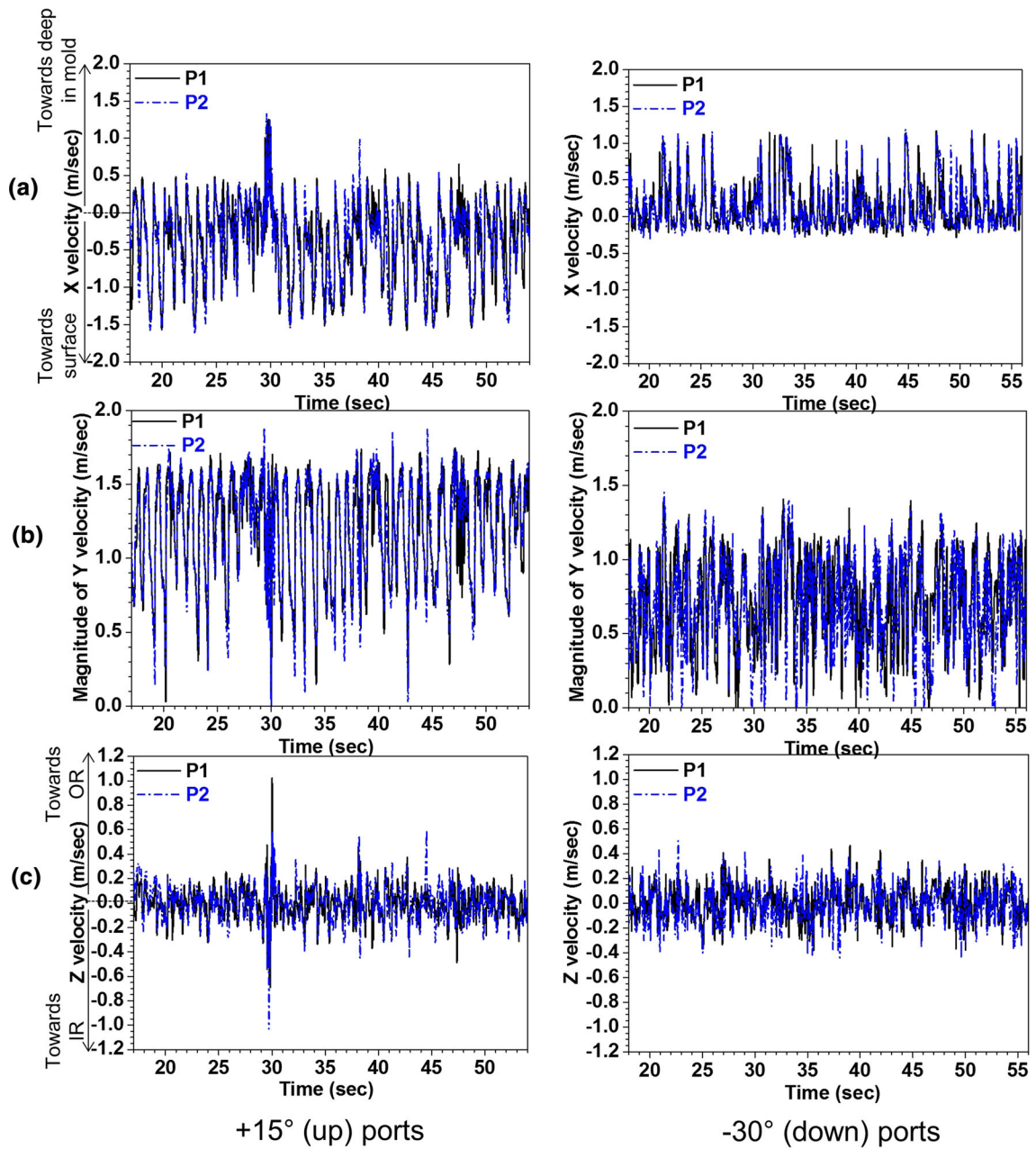
Fig. 9—Comparison of jet velocities (at points P1 and P2) between upward- and downward-angled ports: (a) x velocity (along casting direction), (b) y velocity (toward narrow faces), and (c) z velocity (toward wide faces).

Table V. Jet Flow Characteristics at Points P1 and P2 (Nozzle Port)

	Case 1. + 15 deg (up) (m/s)	Case 2. − 30 deg (down) (m/s)
X velocity		
P1	− 0.40 ± 0.54	0.14 ± 0.32
P2	− 0.39 ± 0.53	0.14 ± 0.32
Y velocity		
P1	1.19 ± 0.35	0.72 ± 0.30
P2	1.19 ± 0.36	0.71 ± 0.30
Z velocity		
P1	− 0.0068 ± 0.13	0.0039 ± 0.13
P2	− 0.0073 ± 0.14	− 0.0057 ± 0.14
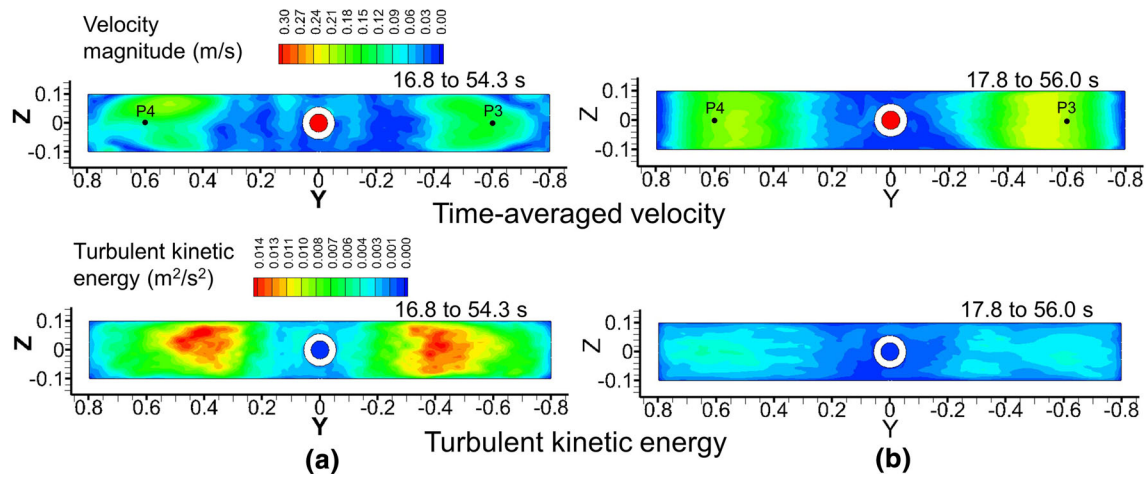
Fig. 10—Time-averaged flow pattern and turbulent kinetic energy at horizontal plane 10 mm below the meniscus for (*a*) + 15 deg (up) ports and (*b*) − 30 deg (down) ports.
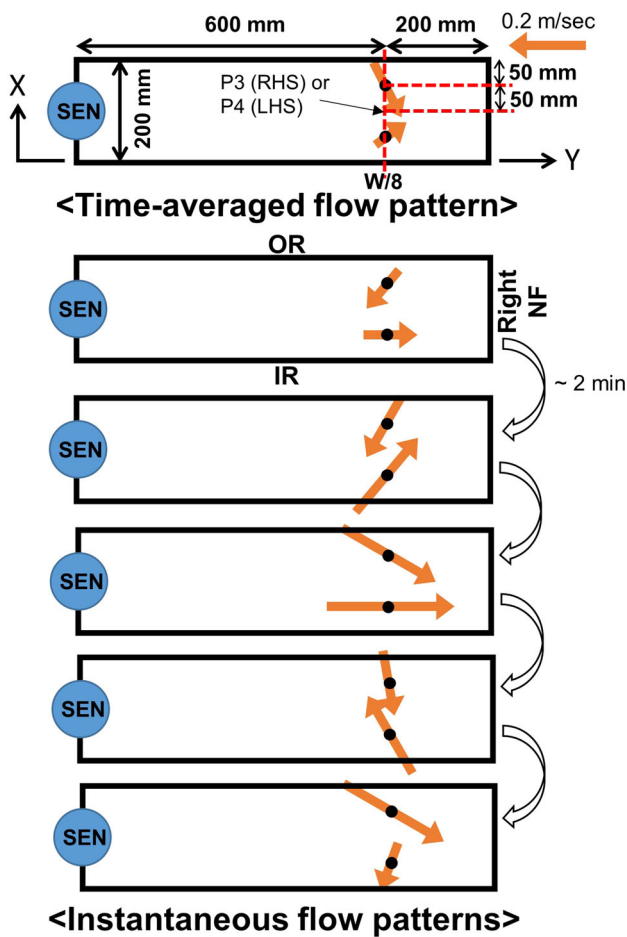
Fig. 11—Measured surface flow patterns from the nail dipping tests: + 15 deg (up) angle nozzle.

slag emulsification). So, it is not surprising that the LES-VOF model calculated much greater slag volume entrapped for the upward ports.

D. *Liquid Mold Flux/Molten Steel Interface Shape*

Nozzle port angle greatly affects the profile of the interface between the liquid mold flux and the molten steel and its time variations. Figure 16 shows the 0.5 volume-fraction mold flux contour, which represents the time-averaged three-dimensional meniscus level (slag/steel interface). Seven cross sections through Figure 16 are shown in Figure 17 (three wide face views) and Figure 18 (four narrow face views). These sections represent the time-average meniscus level profiles, calculated from the instantaneous profiles given in Supplementary Animations 5 and 6. In these figures, zero represents the time and spatial average of the meniscus level, which is 10 mm below the top of the initial liquid layer.

Meniscus profiles are shown across different sections between the two wide faces in Figure 17. The meniscus profiles for both nozzle angles show a strong curvature, contacting the IR and OR at ~ 3 mm lower than the farfield surface level, due surface tension. This is why the IR and OR surface profiles in Figure 17 are generally so much lower than the center section. This meniscus curvature is most obvious at the center between the narrow faces, in the thin channels between the SEN and wide faces. Here, the surface tension suppresses the liquid level by over 4 mm. Meniscus curvature is greatest in the corners, as observed in Figure 16, which agrees with previous studies,[52] and confirms that the current LES-VOF model can make realistic predictions of meniscus behavior.

With upward ports, the highest surface level is found at the quarter-plane location in Figure 18, where the jet flow impinges to make a hump, observed in Figure 16. The hump is more severe near the meniscus on both the IR and OR walls, due to strong upward flow from jet impingement on the wide faces in this region, as shown in Figure 8. Surface level also builds up toward the narrow faces, as jet flow with this nozzle is strong from the hump to the narrow faces.
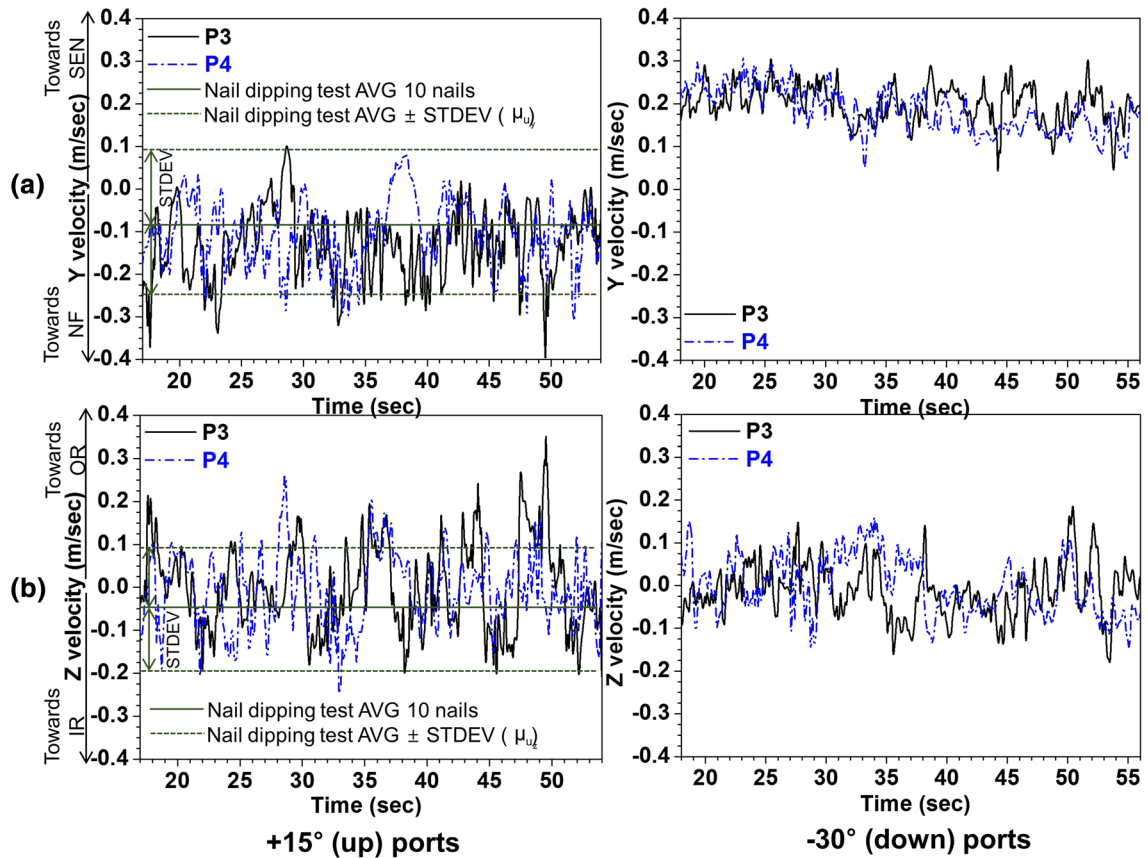
Fig. 12—Comparison of surface velocities (at points P3 and P4) between simulations and measurements for upward and downward nozzles: (a) y velocity and (b) z velocity.

On the other hand, the interface profile experiences a trough (minimum level) between the SEN and narrow face with the downward ports, where surface velocity is highest. High crests are produced near the narrow faces, where the strong upward flow impinges upon the meniscus region. The maximum average difference from crest to trough is ~ 8 mm with this nozzle, which is even higher than the ~ 6 mm maximum profile variation observed with upward ports, due to the generally higher surface velocities associated with the classic double-roll pattern with downward ports.

E. Level Fluctuations

Surface level fluctuations, vertical time variations of the slag/molten steel interface, are shown for both nozzles in Figure 19(a) as $\sigma_{x,}$ standard deviations of the level at the center-middle plane and IR meniscus. The level fluctuations are generally much more severe with upward ports than with downward ports, especially at the meniscus region (IR), as also shown in Figure 19(b). With upward ports, the maximum average level fluctuations are 3.4 mm (within one standard deviation), found roughly midway between SEN and NF, due to unstable wobbling of the jet where it impinges the top surface (see Supplementary Animations 5 and 6). With

downward ports, the maximum level fluctuations are 2.3 mm, found at the meniscus on the right NF, due to asymmetric mold flow causing variations in the vertical momentum up the narrow faces, which indicates slight sloshing behavior at very low frequency (> 18 seconds time period). Figure 20 shows time histories of the slag/molten steel interface level midway between SEN and right NF (400 mm far from the mold center). This figure illustrates how the surface level is higher and more unstable with the upward ports, with instantaneous fluctuations exceeding 10 mm. Further processing of these results in Figure 21 reveals that the power of the surface level fluctuations is strongest at a frequency of ~ 0.12 Hz, which matches the peak in z velocity at the surface, shown in Figure 13(b). This reveals that the surface level fluctuations are caused mainly by variations in surface cross-flow velocity, which generate the largest fluctuations every ~ 8.3 seconds.

F. Slag Entrapment during Level Drops

Figure 22 (snapshots of Supplementary Materials 5 and 6) shows an example of severe meniscus level drops, exceeding 10 mm at the meniscus, which occur where the wobbling jet from the upward ports impinges on the liquid mold flux/molten steel interface. This can result in

Table VI. Surface Flow Characteristics at P3 and P4 (Mold Top Surface)

	Case 1. + 15 deg (up) (m/s)	Case 2. − 30 deg (down) (m/s)
Y velocity		
P3	− 0.130 ± 0.082	0.200 ± 0.042
P4	− 0.100 ± 0.079	0.180 ± 0.052
Z velocity		
P3	− 0.002 ± 0.101	− 0.012 ± 0.061
P4	− 0.007 ± 0.087	0.000 ± 0.068
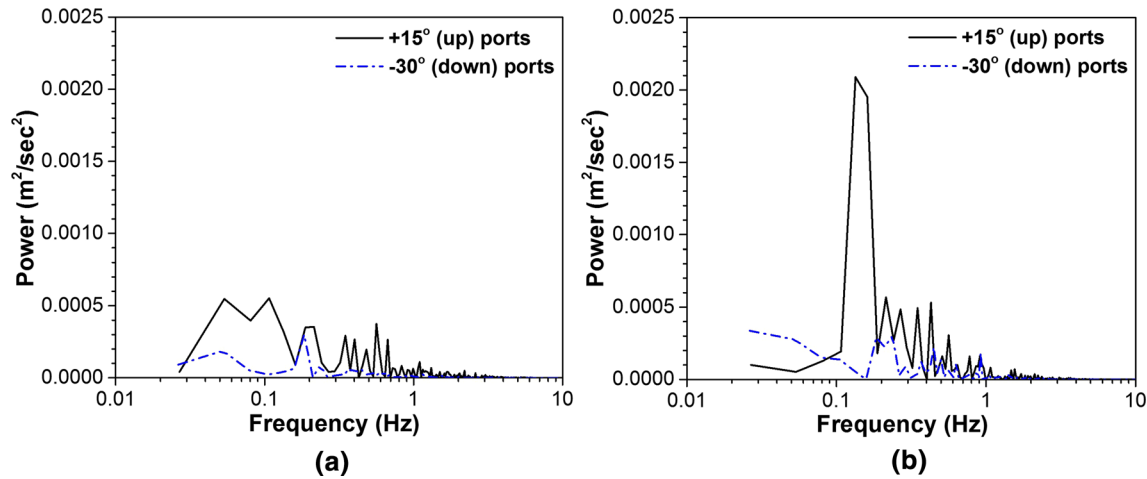
Fig. 13—Comparison of power spectrum of (*a*) *y* velocity and (*b*) *z* velocity fluctuations at P3, between + 15 deg (up) ports and − 30 deg (down) ports.

slag entrapment into the steel shell, especially if hook formation from freezing the meniscus region is severe. At the same time, an open eye is observed, where the liquid mold flux layer divides to enable the molten steel to touch the powder layer. These detrimental phenomena often occur together, as shown in Figure 23. The open eye is a critical product quality problem because it allows both reoxidation of the steel, and carbon pickup from the powder.[53] It is important to note that the small cell vertical size (1 mm) across the slag/molten steel interface and small time step size (~ 0.001 seconds) should be sufficient to track the interface and to quantify its time variations with reasonable accuracy.

Figure 24(a) shows details of the slag entrapment mechanism with level fluctuations. A severe level drop brings the liquid slag in contact with the steel solidification front, where it may become finally entrapped just beneath the surface of the steel shell. Such entrapped slag can cause surface defects, such as shown in Figure 24(b) if the thickness of the surface layer removed by scale formation and expensive subsequent scarfing or grinding operations is insufficient. This entrapment mechanism is particularly problematic for stainless steels, because surface oxidation is so small. Previous plant guidelines for grinding depth have been based on removing a surface layer equal to the maximum hook depth.[54] Based on the level-drop mechanism

in Figure 24(a), a criterion for critical level drop, h_{cr}, which may lead to slag defects can be estimated as follows:

$$h_{cr} = u_{casting}\left(\frac{L_g}{k_c}\right)^2, \qquad [13]$$

where $u_{casting}$ is casting speed, L_g is grinding thickness, and k_c is empirical coefficient used for Eq. [10] to estimate the solidifying steel shell thickness along casting direction. This equation suggests that higher casting speed, larger grinding thickness, and slower shell growth rate increase the critical level drop, which should lessen slag defects based on this mechanism. For the current casting conditions with 1.5 mm of surface thickness removed by grinding the wide faces, the critical level drop is 2.6 mm (WF) and 0 mm (NF). Figure 25 shows average meniscus level, critical surface level, and instantaneous level profiles on both IR and right NF. Five potential instances of slag entrapment are observed in just this single snapshot, which confirms the importance of this mechanism. Figure 26 compares the instantaneous distribution of slag at the IR steel shell front between upward and downward ports, which involves very small volume-fraction contours. The mold cavity for the upward port case is seen to contain much more slag, due to both more
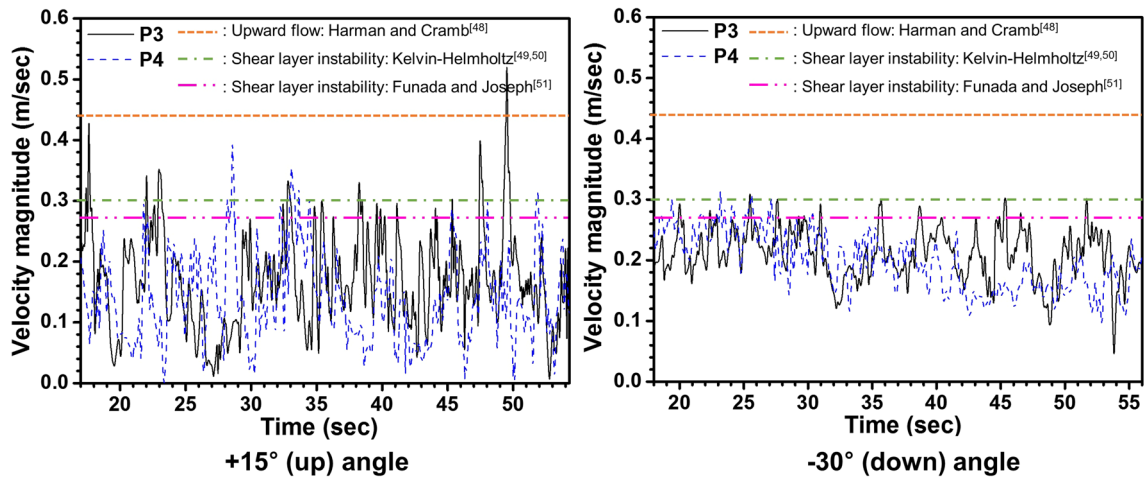
Fig. 14—Comparison of predicted surface velocity magnitude (at points P3 and P4) with the slag entrainment criterions.
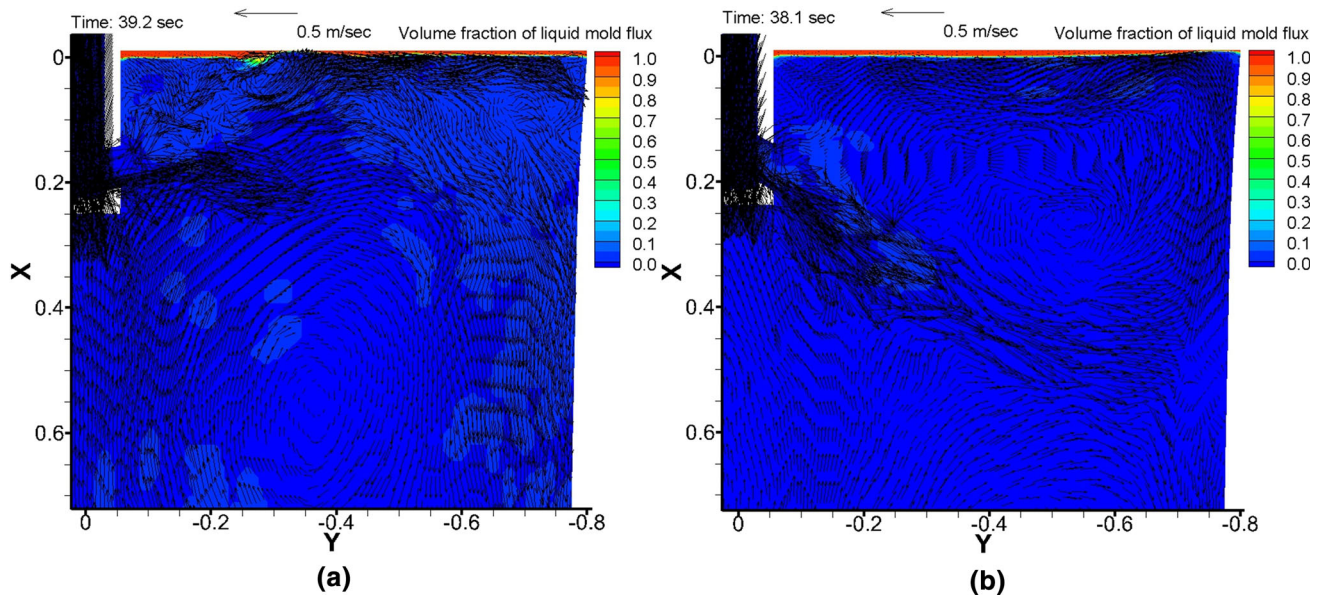

Fig. 15—Instantaneous slag/steel interface behavior at center-middle plane in the mold, comparing (*a*) + 15 deg (up) ports and (*b*) − 30 deg (down) ports.

entrainment and more entrapment near the meniscus. Together with the results in Figures 19 and 20, this work agrees with and explains the plant experience that more surface defects related to mold slag entrapment were found with the SEN with upward ports.

G. *Meniscus Behavior*

Molten steel and liquid mold flux flow behavior near the meniscus in a casting mold significantly affects initial steel solidification, slag consumption into the gap between the solidifying steel shell and the mold hot face, and ultimate surface quality. The overflow of molten steel over the meniscus produces oscillation marks and often also completes the formation of subsurface hooks.[6] In addition, this process may capture slag above the hooks, leading to surface slivers.

As shown in Figure 27, the mold flow pattern, as affected by the nozzle port angle, has some influence on meniscus behavior. With upward ports and flow toward the narrow face, a secondary recirculation region produces upward flow in the meniscus region at the narrow face. At the same time, upward flow near the wide face produces a secondary recirculation region with downward slag flow in the meniscus region at the wide face. With downward ports, the main flow directions and secondary recirculation regions have the exact opposite directions. These recirculation regions may affect meniscus overflow and oscillation-mark depth, but this would require a model with better mesh refinement to study.[55] The increased thickness of the mixture zone of liquid mold flux and molten steel near the top in Figure 27 reveals that more numerical diffusion occurred with the upward-angled nozzle ports,
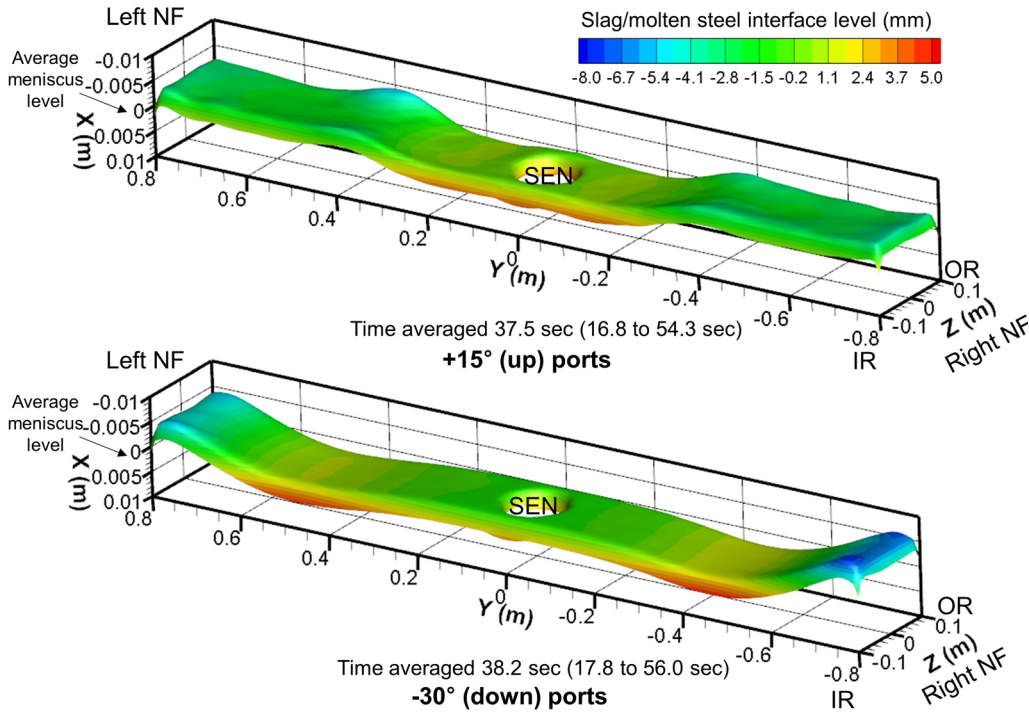
Fig. 16—Comparison of time-averaged 3-dimensional slag/steel interface (liquid mold flux volume fraction: 0.5) in the mold comparing + 15 deg (up) ports and − 30 deg (down) ports: ten-times scaled x-axis (casting direction).
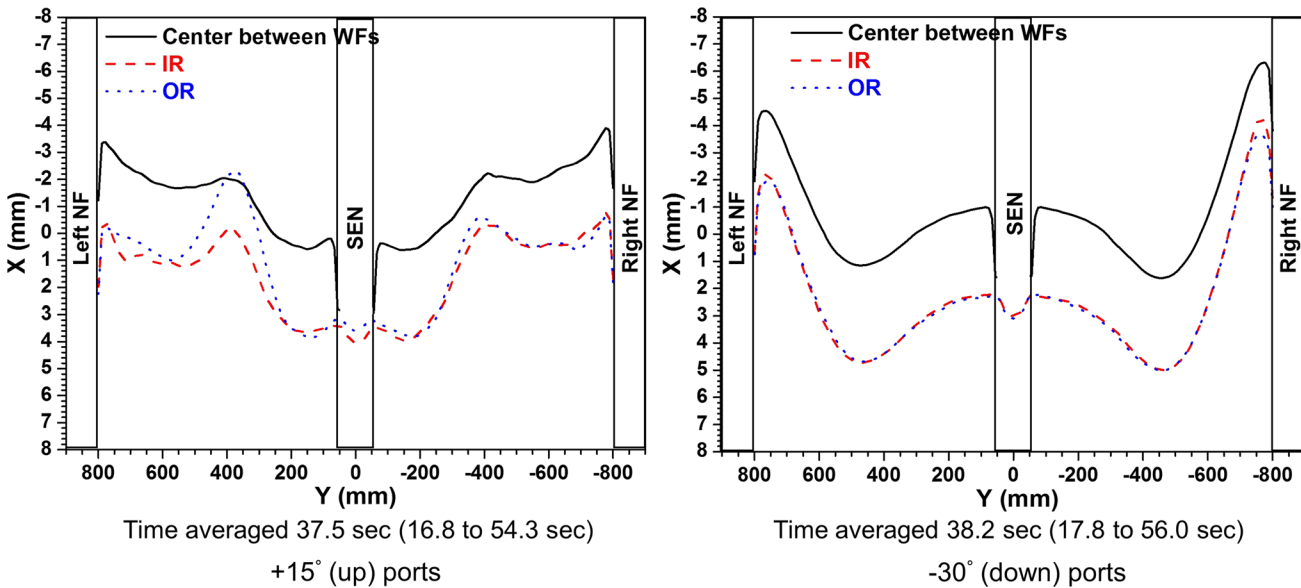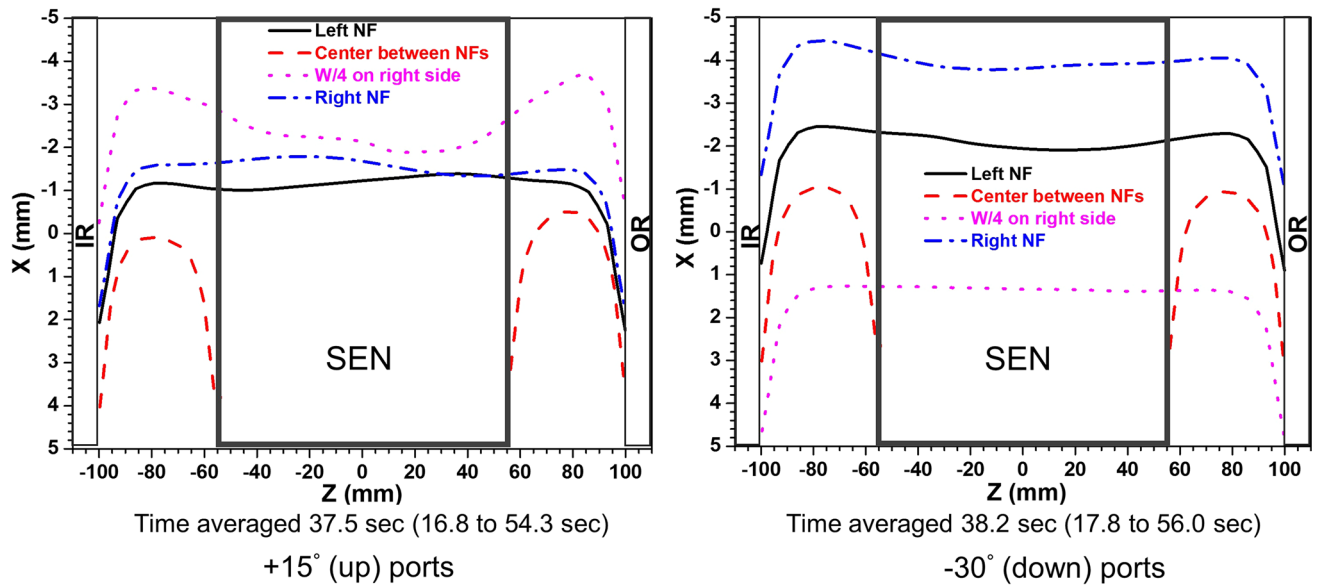

Fig. 17—Comparison of time-averaged slag/steel interface profiles (liquid mold flux volume fraction: 0.5) on front view of wide face in the mold comparing upward and downward ports.

due to more severe level fluctuations in the quarter region between SEN and NF, where the jet flow impinges.

Time average and fluctuations (standard deviations) of the slag/molten steel interface level at the meniscus simulated at the right narrow face for downward ports are compared in Figure 28 with five oscillation-mark profiles measured on the steel slab (Figure 4). The measurement conditions are similar, except for having larger mold thickness (250 mm), slightly narrower mold width (1500 mm), and slightly steeper nozzle ports (− 35 deg). The predicted meniscus level, including both the time average (red dash-dot line) and fluctuations (red error bars), agrees reasonably well with the measurements (black solid lines). Both the simulation and measurements show reasonably horizontal profiles,

Fig. 18—Comparison of time-averaged slag/steel interface profile (liquid mold flux volume fraction: 0.5) on narrow face view (side view) in the mold comparing upward and downward ports.
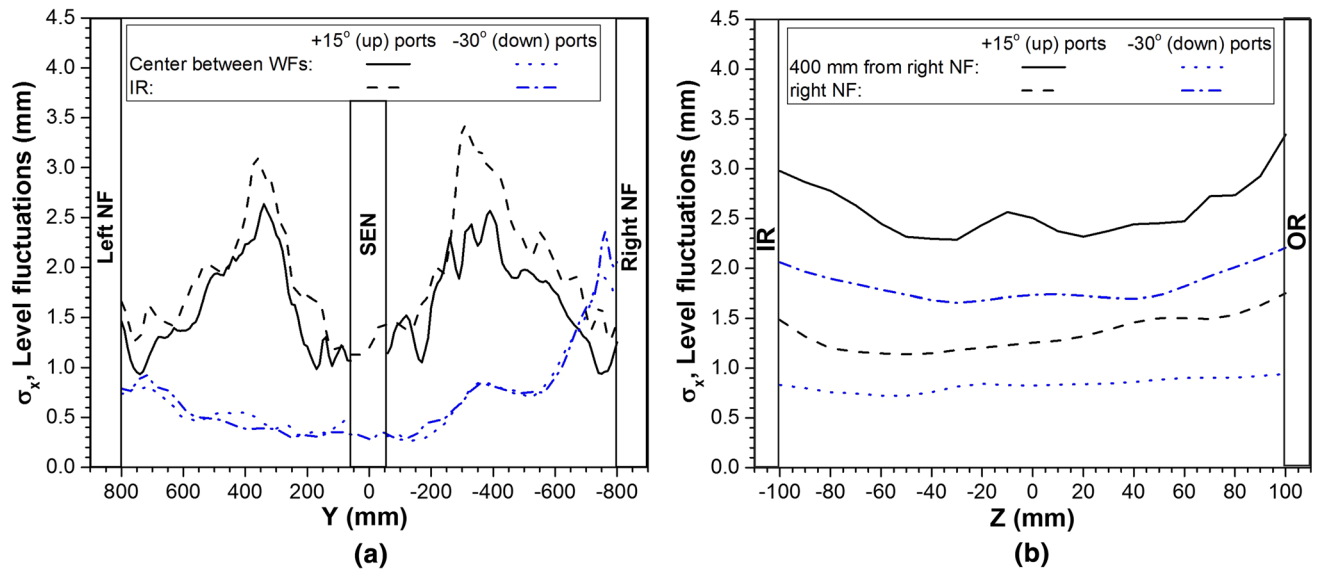

Fig. 19—Comparison of level fluctuations of slag/steel interface (liquid mold flux volume fraction: 0.5) on (*a*) wide face view (front view) and (*b*) narrow face view (side view) comparing upward and downward ports: upward-ports case (for 18 s) and downward-ports case (for 19 s).

with variations of ± 2 mm, except near the corners, where the levels dip down much further, as explained previously. This further validates the LES-VOF model. The measured oscillation-mark profiles in the corner region near the OR are consistently much lower than near the IR. In a similar manner, the simulated left NF profile is consistently lower than the right NF profile. This shows that asymmetric flow can persist for many oscillation cycles, producing regions of deeper oscillation marks which are fundamentally rooted in chaotic turbulent behavior.

VI. ASSESSMENT OF LES-VOF MODEL COMPARED WITH RANS MODEL

Finally, the flow pattern, turbulence contours, surface velocity, and surface level profiles predicted from the LES coupled with VOF model simulations were compared with fast single-phase calculations using a three-dimensional RANS-based standard k-ε model,[56] which is described in previous work.[57] The RANS model was solved with ANSYS FLUENT,[34] adopting the exact same LES-domain geometry, except that two-fold symmetry is assumed so only one quarter of
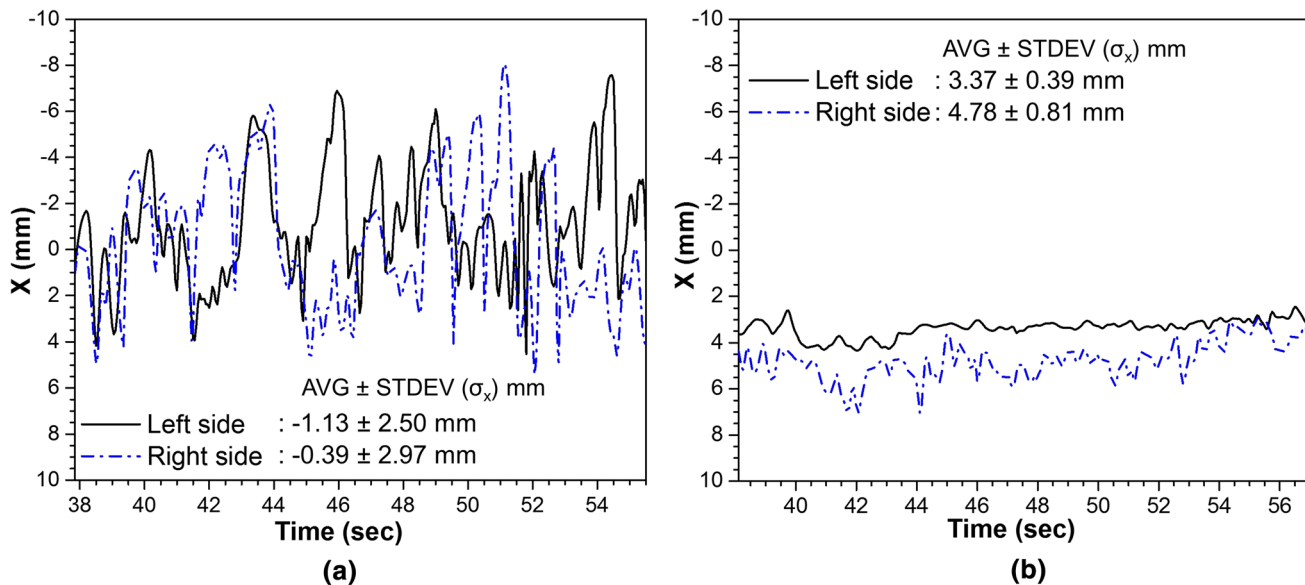
Fig. 20—Time histories of slag/steel interface level (liquid mold flux volume fraction: 0.5) in meniscus regions (both left and right) 400 mm far from the mold center with (a) upward and (b) downward ports.
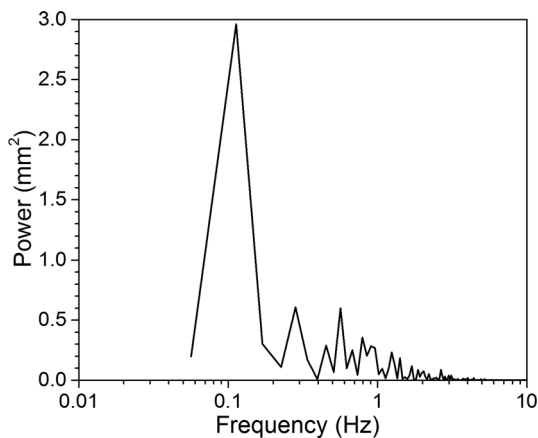

Fig. 21—Power spectrum of level fluctuations of instantaneous slag/steel interface (liquid mold flux volume fraction: 0.5) at IR meniscus 400 mm (right side) far from mold center with upward ports.

the domain is simulated, the slag layer is neglected, and only ~ 0.3 million hexahedral cells are needed. The same process conditions are simulated (Table I), for the upward-ports case. The same boundary conditions were applied as well, including the mass and momentum sink terms to account for solidification, except for additional conditions on k and ε. Specifically, small levels of turbulent kinetic energy (10^{-5} m^2/s^2) and turbulent kinetic energy dissipation rate (10^{-5} m^2/s^3) were set at the inlet surface of the tundish-bottom region, and for back flow entering the domain exit. The no-slip condition at the top surface, representing the interface with the liquid slag is reasonable, considering the ~ 30 × higher dynamic viscosity of the liquid mold flux compared to the molten steel, given in Table II. Each RANS simulation takes only ~ 6 hours of wall-clock time on a workstation (Dell T7600 with E5-2603 1.80GHz CPU, 72 GB, using 6 cores), which is much faster than the

LES simulations on the Blue Waters supercomputer (with 96 cores), which took ~ 24 hours of wall-clock time for 1.5-second flow time; (57 seconds for each 0.001-second time step).

A. Flow Pattern

Figure 29 shows time-averaged mold flow pattern and turbulent kinetic energy in the mold with the upward-angled nozzle ports, from both the transient LES coupled with VOF model and three steady-state standard k-ε RANS-model simulations, using different upwind schemes. Both the LES-VOF model and the standard k-ε models show a single-roll flow patterns and they reasonably match with each other. However, the RANS-model jets are thinner and more downward in the center-middle plane between WFs. This is because real transient jet wobbling is not captured by the steady RANS models. In the y–z plane, however, the RANS-model jets spread more, due to excessive momentum diffusion, reaching the meniscus only 0.2 m from the SEN, vs ~ 0.4 m from the SEN for the LES model (compare top frames in Figure 28). More importantly for defect formation, there is less evidence of impingement onto the top surface with the RANS-model jets. This is partly a consequence of time-averaging, as even the LES model time-average flow pattern does not show the direct impingement on the top surface that is observed in the instantaneous flow-pattern snapshots such as shown in Figure 15(a).

B. Turbulence

Figure 29 also shows that the TKE in the nozzle bottom region, predicted by the standard k-ε models, is much smaller than the LES prediction. This is because the symmetry prevents the formation of steady swirl in
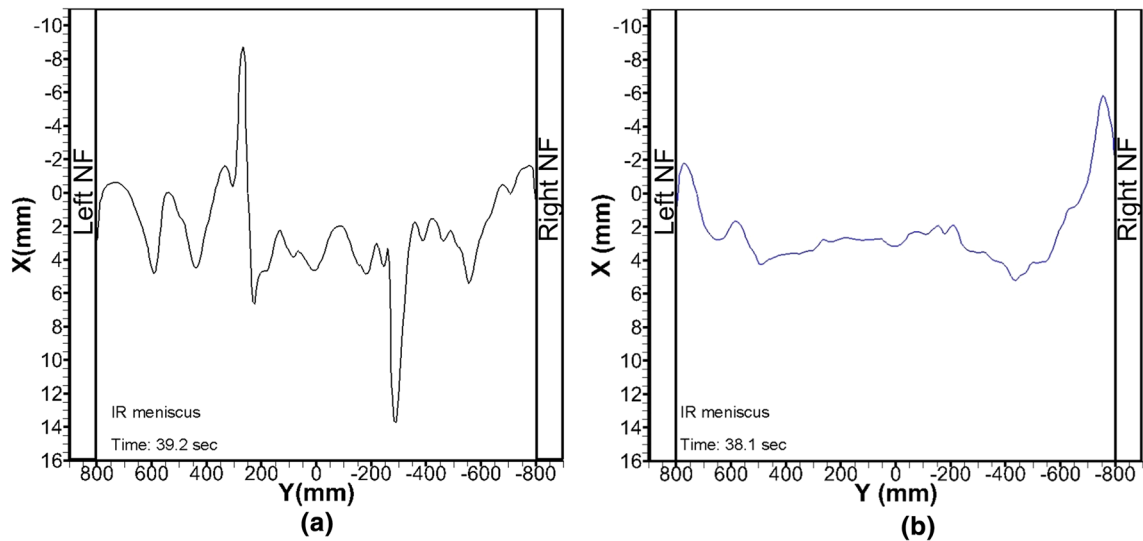
Fig. 22—Comparison of instantaneous slag/steel interface profiles at meniscus for (*a*) + 15 deg (up) ports and (b) − 30 deg (down) ports.
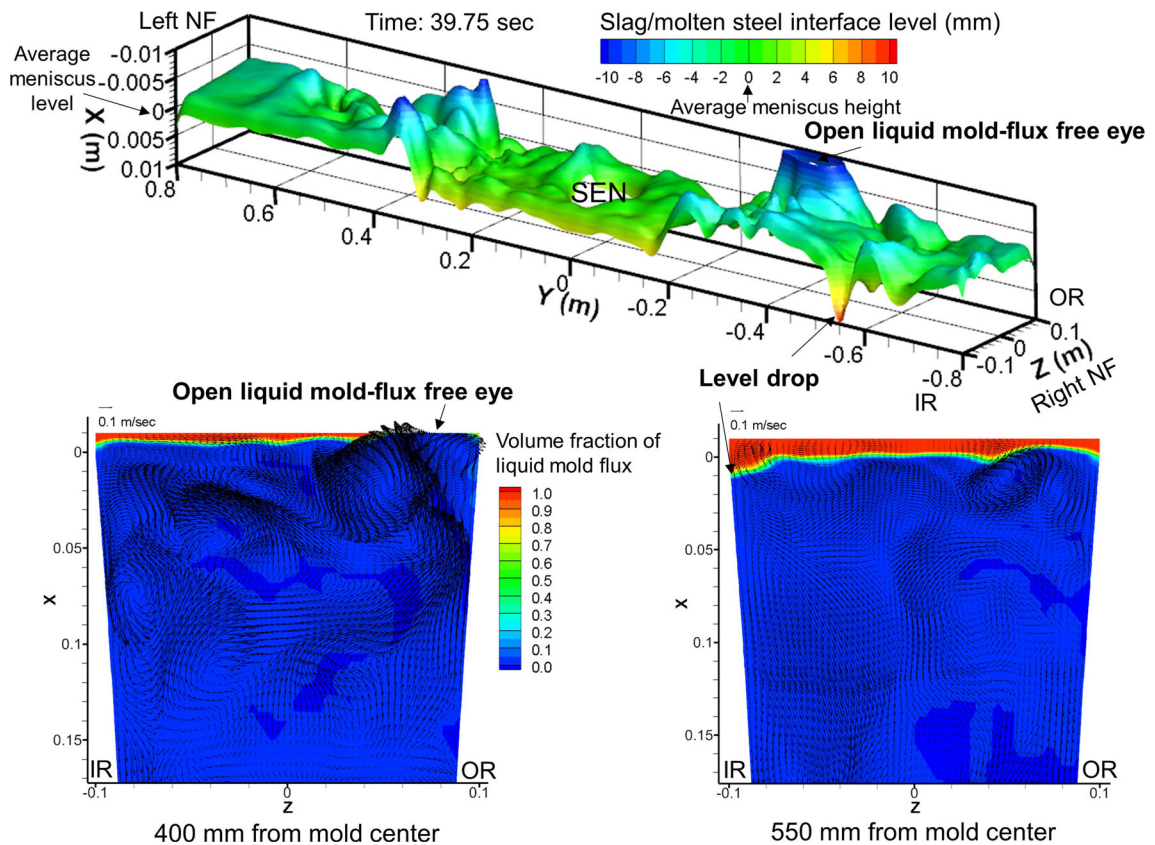

Fig. 23—Instantaneous slag/steel interface drop and open liquid mold flux free eye in the mold with + 15 deg (up) ports: ten-times scaled *x*-axis (casting direction) for three-dimensional interface profile.

this region. The TKE mostly consists of the velocity variations due to changes in the swirl rotation direction, captured by the LES model. The standard *k*-*ε* model with 1st order upwind scheme of momentum term and 2nd order upwind scheme of turbulent kinetic energy term matches best with the LES-VOF model, for time-average flow. The numerical diffusion of case

Figure 29(c) with 1st order upwind scheme of momentum term (together with 2nd order upwind scheme of TKE term) makes the jet slightly thicker than the other RANS cases, which partly offsets the inability of RANS to model jet wobbling. These findings agree with previous studies which compared RANS-model predictions with measurements in lab scale models.[29,58]

C. Surface Velocity

The predicted surface velocity components (Y velocity: toward SEN, Z velocity: toward OR) and their fluctuations are compared with the measurements from the nail dipping tests in Figure 30. Surface velocity fluctuations from the RANS-model simulations were calculated from the turbulent kinetic energy k, assuming isotropic behavior as follows:

$$\text{RMS of } u_y' = \text{RMS of } u_z' = \sqrt{\overline{(u_i')^2}} = \sqrt{\frac{2}{3}k}. \quad [14]$$

Both the LES and RANS models reasonably match with the time-averages of the measured velocity profiles. However, the LES-VOF model better captures the high magnitude of the real fluctuations at the mold surface, represented by the error bars. This is likely that the RANS-model predictions of turbulent fluctuations near the interface are deficient, because velocity variations across the symmetry planes are suppressed, including both cross-flow between WFs and sloshing between NFs.

D. Surface Level Profile

To compare the liquid mold flux/molten steel profiles predicted from the LES-VOF simulation with the single-phase RAN modeling, time-averaged surface level profile, h_i, is calculated from static pressure distribution predicted using the RANS model, as follows:[14]

$$h_i = \frac{P_i - P_{\text{avg}}}{[\rho_s - (1 - c)\rho_f]g}, \quad [15]$$

where P_i is static pressure at location i, P_{avg} is spatial-averaged pressure across the mold surface, and c is a constant to quantify the extent of slag displacement due to density differences relative to vertical motion (i.e., lifting) of the slag/molten steel interface. Assuming the constant $c = 0$ means that slag motion is caused only by displacement of slag by molten steel, as gravity causes some slag to flow down to where the steel level profile is lower and away from where the steel level is higher. A constant of $c = 1$ means that
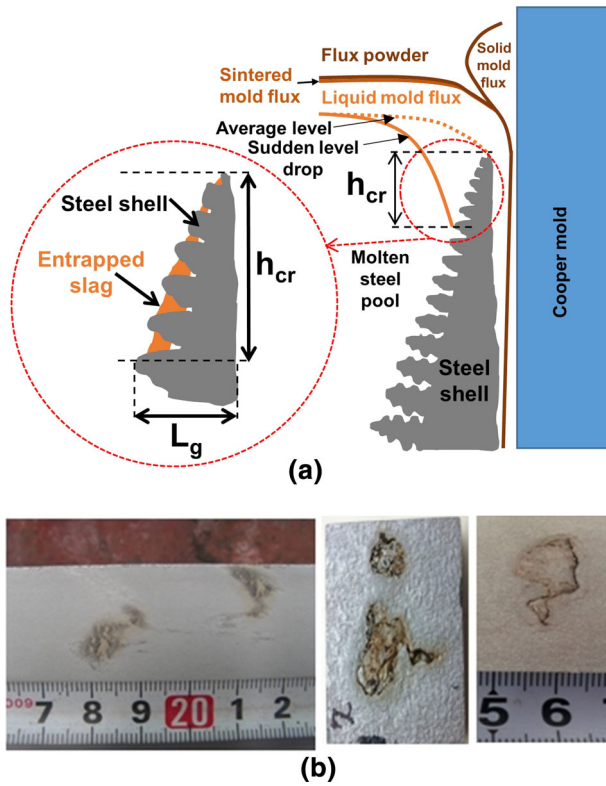
Fig. 24—(a) Schematic of slag entrapment near meniscus and (b) surface defect caused by slag entrapment into the steel shell in the mold with + 15 deg (up) angled nozzle ports.
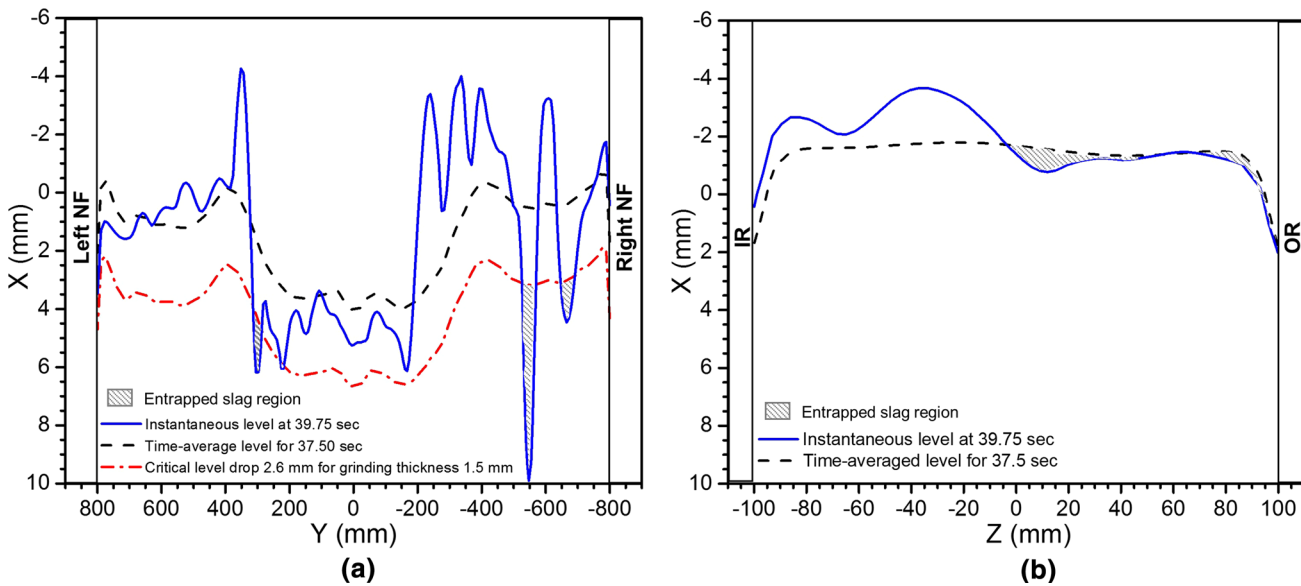
Fig. 25—Predicted slag entrapment into solidifying steel shell on (a) IR and (b) right NF with + 15 deg (up) angled nozzle ports.
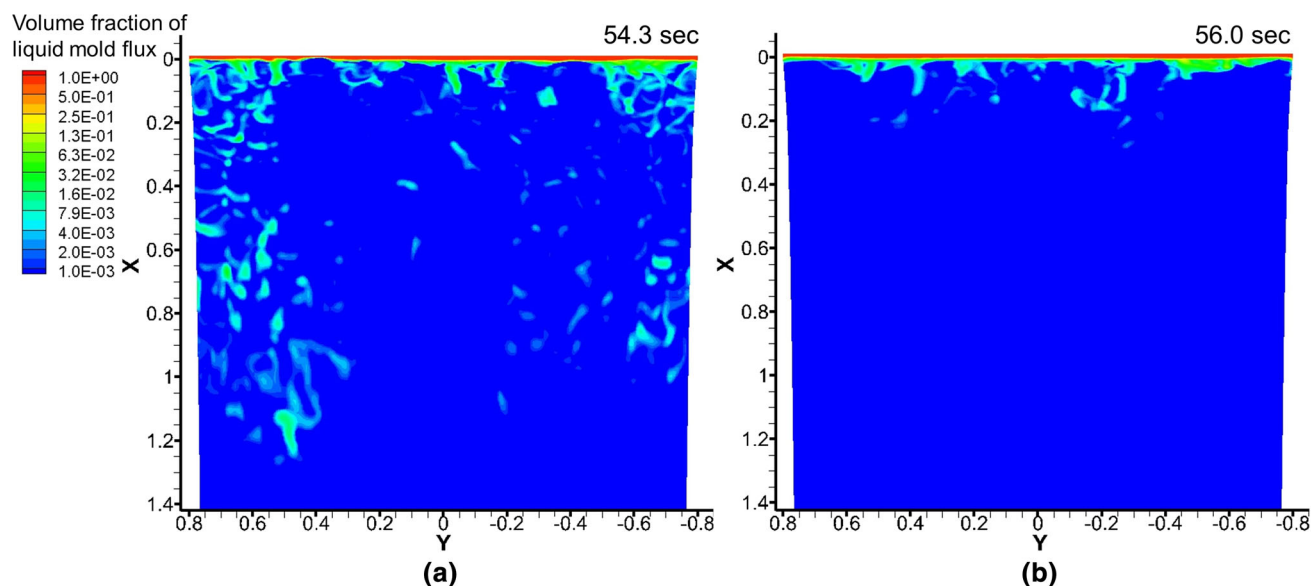
Fig. 26—Comparison of instantaneous slag distribution at the steel shell front on IR for (a) + 15 deg (up) ports and (b) − 30 deg (down) ports.

the slag is simply lifted up and down by the local steel level motion, with no change in the liquid-slag layer thickness. This constant was previously quantified as an empirical coefficient to match plant measurements.[59]

Figure 31 shows predicted interface profiles across the mold surface from the RANS and the LES-VOF simulations. The surface level profiles all generally agree, except for the slight hump in the LES-VOF profile at ~ 400 mm, where the jet flow impinges, which is not captured by the RANS models. This is a natural consequence of the flow-pattern differences. The RANS models also miss the sharp level drops at the meniscus regions, due to their neglect of surface tension.

The RANS with the slag-displacement model ($c = 0$) shows better agreement with the LES-VOF model, with a steeper slope from SEN to right NF. Considering that the LES model should be more accurate, and agrees better with plant measurements,[14,59] this finding appears to contrast with previous work that showed better agreement with the slag-lifting model. This is explained, however, as vertical lifting of the liquid-slag layer, such as during relatively rapid level fluctuations measured in previous work,[14,59] occurs in short time scales, while longer times, of greater interest in this work, are likely needed to enable the slow-flowing slag to develop significant slag displacement.

E. Comparison with Previous Water Model Study

Previous work has shown that single-phase flow in water models generally matches that in commercial casters, except near the top surface, due to the effects of the slag layer, and in thin-slab casters, due to upward deflection of the jet by the solidifying steel shell, which

takes up a significant fraction of the thickness cross section.[60,61] In this work, both the computational model predictions of the plant and the plant measurements show a single-roll flow pattern for the upward-ports case, as shown in Figure 30(a). This contrasts with previous results from a 1/3-scale water model for the exact same conditions, in which both the water model measurements and RANS simulations showed double-roll flow patterns (see Figure 14 in Cho et al.).[26]

This finding that the flow pattern in the water model is opposite from that observed in the plant measurements may be explained by two reasons. Besides the scale factor and minor differences in fluid properties, the only differences were neglect of the slag layers and the solidifying steel shell. Although the effect of the curved shape of the solidifying shell is usually small in a thick-slab caster, its effect of upward deflection was apparently enough to change the flow pattern in this case. This is likely because the jet from the upward ports spreads to impinge strongly onto the wide faces, so can be deflected further upward, and because the flow pattern for this case is somewhat unstable and near to changing directions. Perhaps the free surface movement of the water model contributed as well. All of the results in both works agree that surface velocities are higher with the downward ports, but surface level fluctuations/turbulence are higher with the upward ports.

It should be emphasized that the simulations match well with the measurements for both the real caster and water model cases. For the real caster case, the LES-VOF and the RANS models both predict the single-roll pattern measured in the plant case. The RANS model matched well with the double-roll pattern in the water model case. These findings reveal that
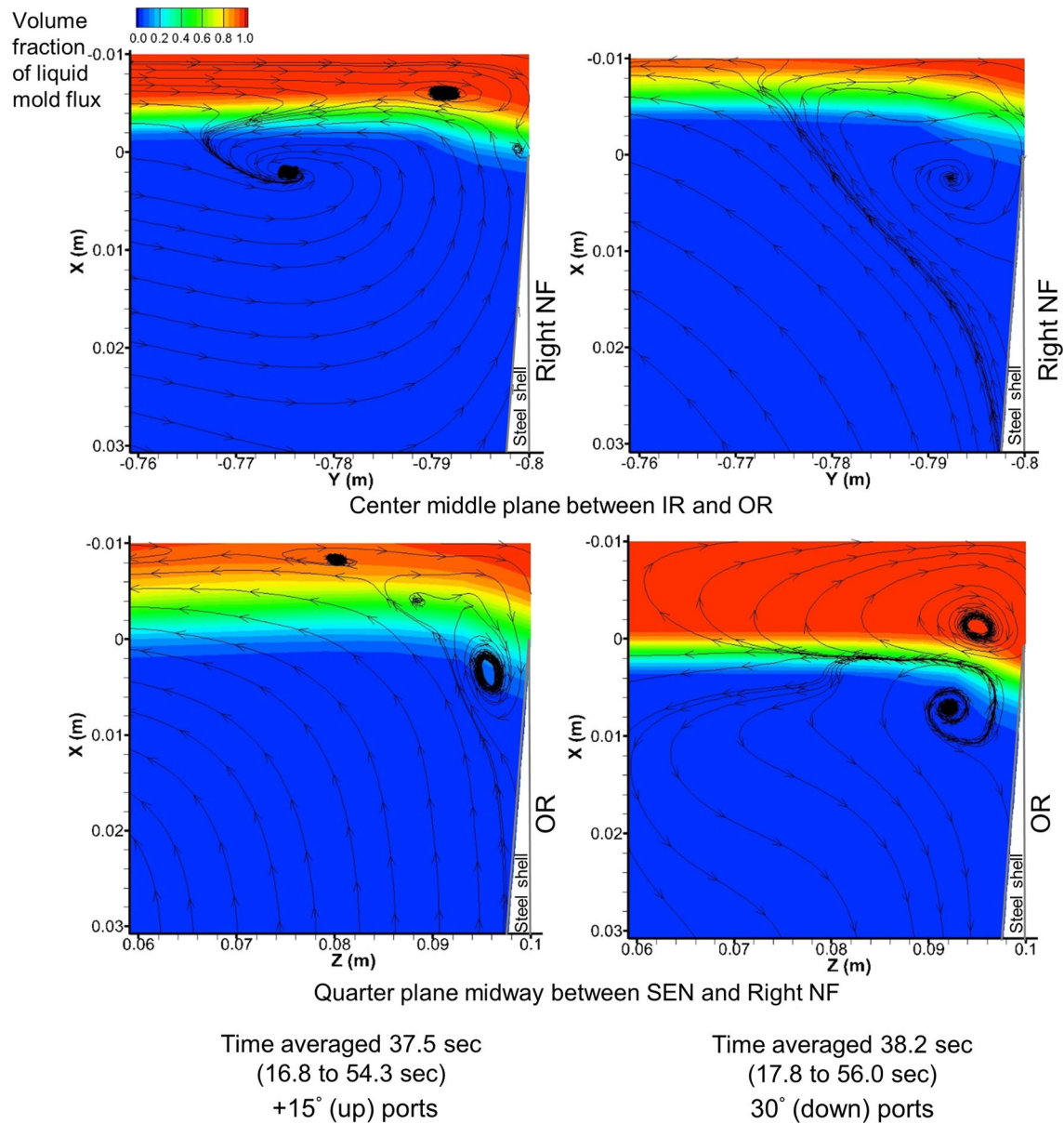
Fig. 27—Time-averaged flow patterns near the meniscus in the mold for + 15 deg ports and − 30 deg ports.
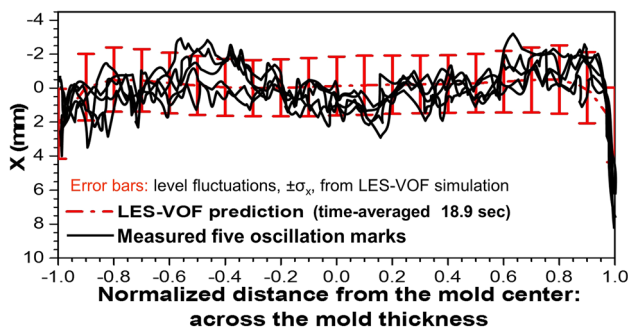

Fig. 28—Comparison of the predicted meniscus profile (LES-VOF model prediction) with measured oscillation marks profiles on right narrow face with downward-angled nozzle ports.

computational modeling is an ideal tool to quantify complex flow in continuous casting.

VII. SUMMARY AND CONCLUSIONS

The effect of nozzle port angle on transient turbulent flow phenomena in a nozzle and mold with stopper-rod flow control is investigated using a three-dimensional LES model coupled with VOF. The model is validated with plant measurements of surface velocity and oscillation-mark profiles and applied to evaluate nozzle and mold flow patterns, liquid mold flux/molten steel interface motion, slag entrapment, and meniscus behavior during nominally steady continuous steel-slab casting. The main findings are as follows:
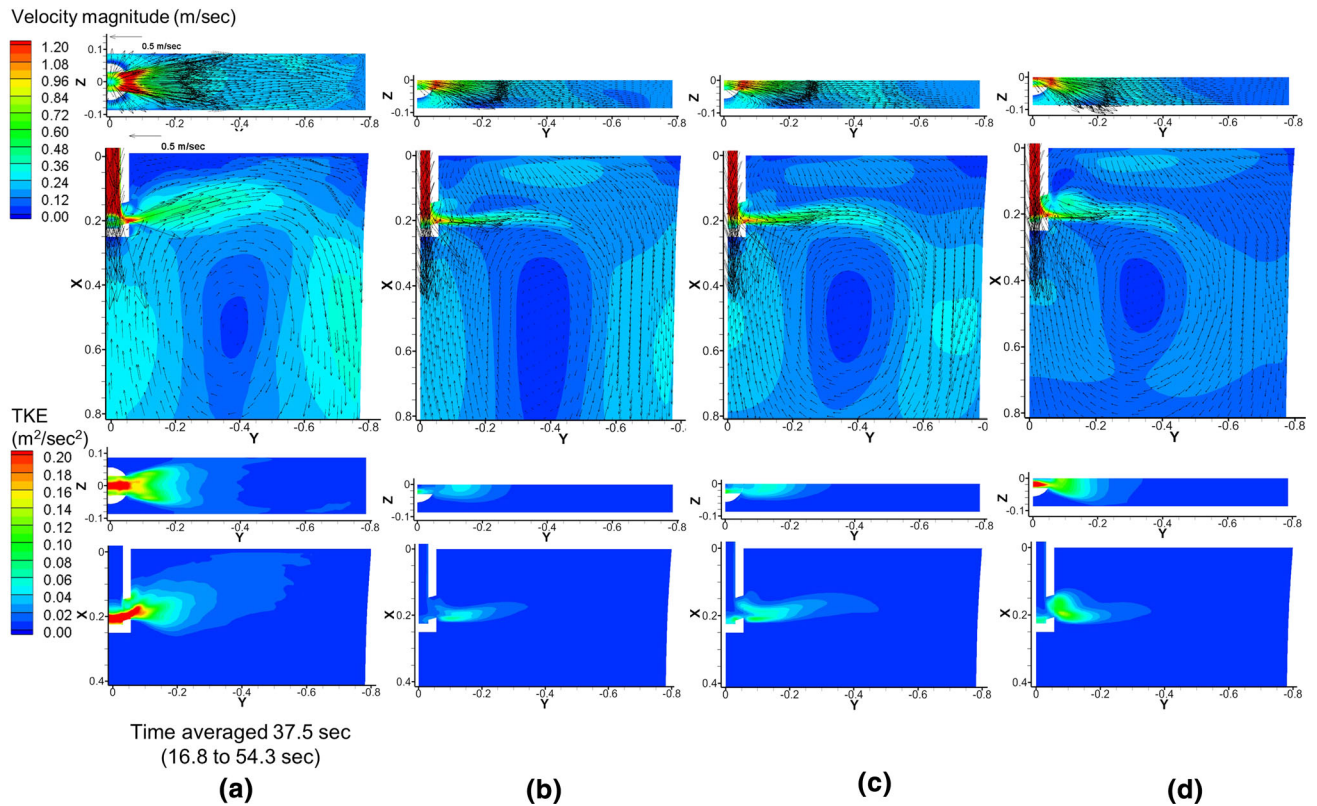
Fig. 29—Comparison of time-averaged flow pattern and TKE at cross-sectional plane 200 mm below meniscus and center-middle plane in the mold with + 15 deg (up) ports: (*a*) LES coupled with VOF model, standard *k*-*ε* model with (*b*) 1st order upwind schemes, (*c*) 1st order upwind scheme of momentum and 2nd order upwind scheme of TKE, (*d*) 2nd order upwind schemes.
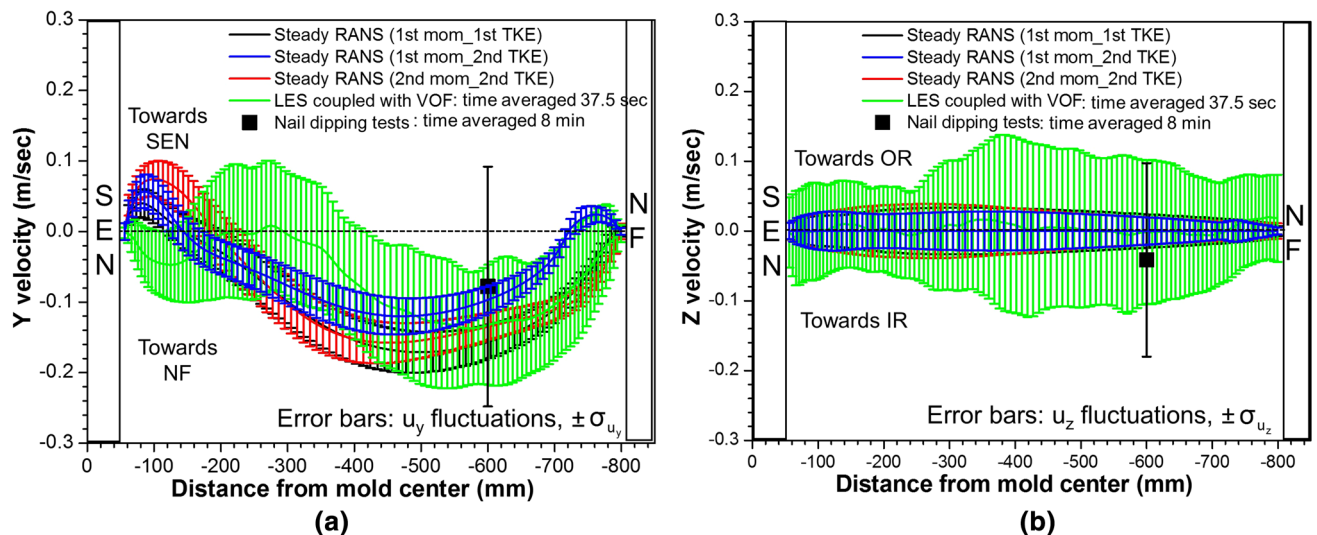

Fig. 30—Comparison of surface velocity components in the mold (10 mm below the steel-slag interface) with + 15 deg (up) ports comparing model predictions and measurements: (*a*) velocity toward SEN and (*b*) velocity toward OR.

1. Averaged flow parameters at nozzle exit, such as jet and spread angles, can characterize the important effect of nozzle geometry on flow entering the mold.
2. Jet flow from the nozzle with upward-angled ports produces a single-roll pattern with jet impingement on the top surface midway between the SEN and NF,

where the highest surface level and greatest level fluctuations are produced. Larger momentum diffusion with a broader jet across the mold thickness results in slightly lower surface velocities and a flatter surface profile, compared to the nozzle with downward-angled ports.
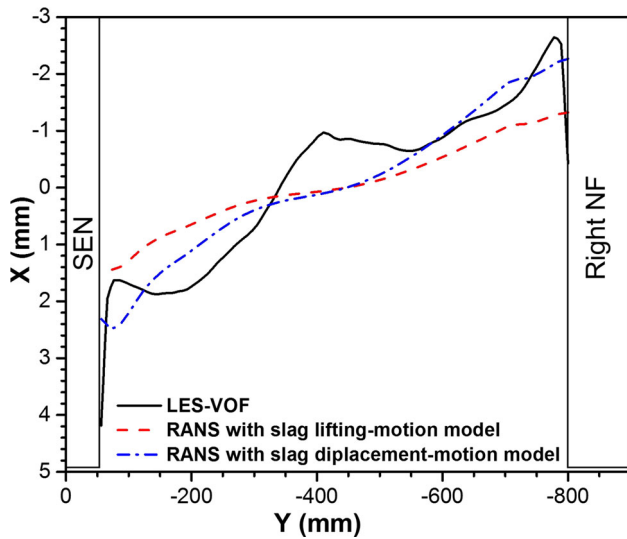
Fig. 31—Comparison of slag/steel interface profiles at the center-middle plane between IR and OR in the mold with + 15 deg (up) ports comparing the model predictions.

3. The downward ports generate a classic double-roll flow pattern with a strong, high-momentum jet and flow up the narrow face that impinges on the narrow face meniscus, where it produces a crest in the level profile and maximum in level fluctuations. The highest surface velocity is across the center region, midway between the SEN and NF, where it produces a trough in surface profile.

4. The single-roll flow pattern from the upward ports leads to severe surface level fluctuations, due to strong variations in surface cross-flow velocity between WFs. Sudden severe level drops of over ~ 10 mm were predicted, which likely increase the chances of the slag entrapment into the initial solidifying steel shell, especially on the WFs near the quarter plane. Results from a new model based on entrapped slag depth corresponding with level drops suggest that 1.5 mm of grinding is insufficient to remove surface slag for the stainless-steel slabs and casting conditions investigated here.

5. The LES-VOF model shows reasonable agreement with plant measurements of surface velocity from nail dipping tests and meniscus level profiles from oscillation-mark profile measurements.

6. Comparison with results from a standard k-ε turbulence model shows that such RANS-based flow models can reasonably predict time-averaged flow and surface velocity magnitude. First-order upwinding for momentum appears to be best, as the extra numerical diffusion partly compensates for underprediction of jet wobbling. However, surface flow impingement and velocity fluctuations are still underpredicted, due to inability to capture asymmetric flow. The simple slag-displacement model based on surface pressure variations compares well with the full LES -VOF model results.

7. Comparison with previous results from a 1/3-scale water model, in which both measurements and RANS simulations showed double-roll flow patterns, differs from the current work for the upward-ports case, in which both the measurements and models show a single-roll flow pattern. This is likely due to the water model missing the solidifying steel shell and the top surface slag layer.

APPENDIX: SPREAD ANGLES OF JET FLOW

Vertical and horizontal spread angles of the jet flow at the nozzle port outlet are calculated to quantify the flow characteristics leaving the nozzle. The calculation is based on a weighted average of outward flow rate, ignoring the backflow zone where flow enters the port. Figure A1 illustrates the definition of both spread angles.

Vertical spread angle, $\theta_{xy,sp}$ is calculated as follows:

$$\theta_{xy,sp} = |\theta_{xy} - \theta_{xy,upper}| + |\theta_{xy} - \theta_{xy,lower}|, \qquad [A1]$$

where θ_{xy} is the vertical jet angle at the nozzle port outlet surface,[25,46] $\theta_{xy,upper}$ and $\theta_{xy,lower}$ are vertical jet angles calculated from the velocity vectors leaving each region, split into upper and lower regions according to the regions of the port exit surface found above and below the center plane of the jet flow, respectively. Due to the back flow zone located in the upper part at the nozzle port outlet, the two regions are separated, based on a mass flow-rate balance of the jet as follows:

$$\sum_{i=1}^{N-n}(\Delta x)_i(\Delta z)_i u_{mag,i} = \sum_{j=1}^{n}(\Delta x)_j(\Delta z)_j u_{mag,j}, \qquad [A2]$$

where i and j are cells in the upper and the lower port regions, respectively, (numbered according to
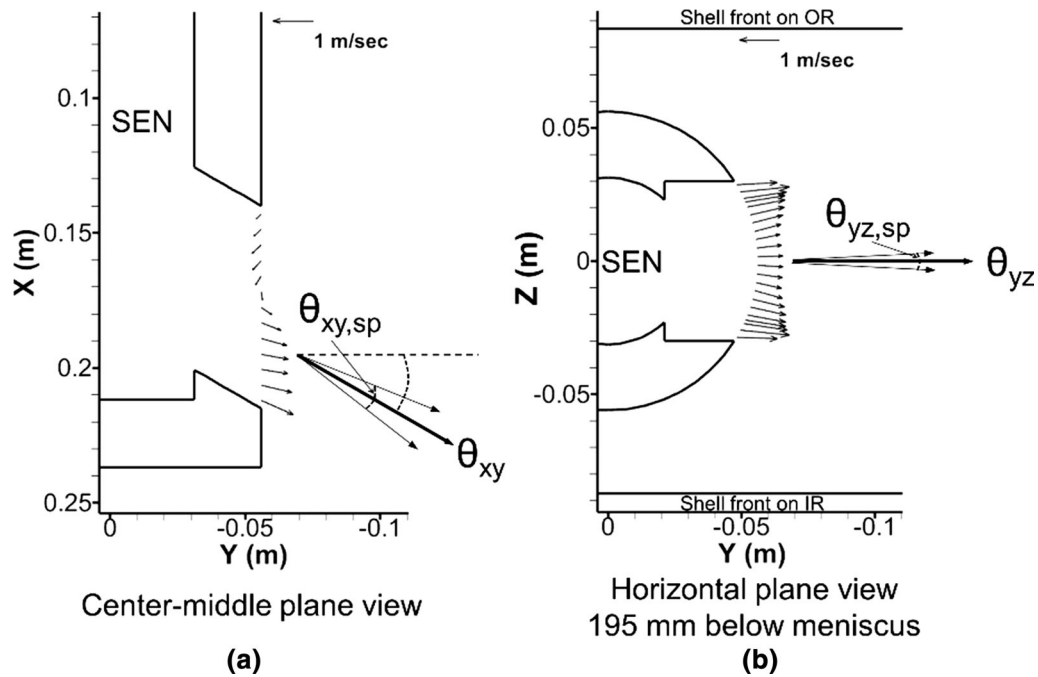
Fig. A1—Definition of (*a*) vertical spread angle and (*b*) horizontal spread angle of jet flow: example of downward-angled nozzle ports.

increasing x height when calculating vertical spread angle), N is the total number of cells in the jet region with positive outflow, n is the unknown total number of cells in the lower region to be solved, and u_{mag} is the velocity magnitude in each cell in the exit plane of the nozzle port.

Horizontal spread angle, $\theta_{yz,sp}$, is calculated in a similar manner, as follows:

$$\theta_{yz,sp} = \left| \theta_{yz} - \theta_{yz,IR} \right| + \left| \theta_{yz} - \theta_{yz,OR} \right|, \quad [A3]$$

where θ_{yz} is the horizontal jet angle at the nozzle port outlet surface,[25,46] $\theta_{yz,IR}$ and $\theta_{yz,OR}$ are the horizontal jet angles in each ~ half-port region, IR and OR side, respectively.

ELECTRONIC SUPPLEMENTARY MATERIAL

The online version of this article (https://doi.org/10.1007/s11663-018-1439-9) contains supplementary material, which is available to authorized users.

REFERENCES

1. L.C. Hibbeler and B.G. Thomas: *Iron Steel Technol.*, 2013, vol. 10 (10), pp. 121–36.
2. T. Teshima, M. Osame, K. Okimoto and Y. Nimura: *Proc. of 71th Steelmaking Conf.*, The Iron and Steel Society, London, UK, 1988, pp. 111–118.
3. M. Iguchi, J. Yoshida, T. Shimizu, and Y. Mizuno: *ISIJ Int.*, 2000, vol. 40, pp. 685–91.
4. R. Hagemann, R. Schwarze, H.P. Heller, and P.R. Scheller: *Metall. Mater. Trans. B*, 2013, vol. 44B, pp. 80–90.
5. H. Shin, S. Kim, B.G. Thomas, G. Lee, J. Park, and J. Sengupta: *ISIJ Int.*, 2006, vol. 46, pp. 1635–44.
6. J. Sengupta, B.G. Thomas, H. Shin, G. Lee, and S. Kim: *Metall. Mater. Trans. A*, 2006, vol. 37A, pp. 1597–1611.
7. Z. Liu, B. Li, and M. Jiang: *Metall. Mater. Trans. B*, 2014, vol. 45B, pp. 675–97.
8. Z. Liu, F. Qi, B. Li, and M. Jiang: *J. Iron Steel Res. Int.*, 2014, vol. 21, pp. 1081–89.
9. Z. Liu, Z. Sun, and B. Li: *Metall. Mater. Trans. B*, 2017, vol. 48B, pp. 1248–67.
10. S.-M. Cho, S.-H. Kim, R. Chaudhary, B.G. Thomas, H.-J. Shin, W.-Y. Choi, and S.-K. Kim: *Iron Steel Technol.*, 2012, vol. 9, pp. 85–95.
11. R. Chaudhary, G.-G. Lee, B.G. Thomas, S.-M. Cho, S.-H. Kim, and O.-D. Kwon: *Metall. Mater. Trans. B*, 2011, vol. 42B, pp. 300–15.
12. C. Ojeda, B. G. Thomas, J. Barco, and J. L. Arana: *Proc. of AISTech 2007*, Assoc. Iron Steel Technology, Warrendale, PA, USA, 2007, vol. 1, pp. 269–84.
13. J. Sengupta, C. Ojeda, and B.G. Thomas: *Int. J. Cast Met. Res.*, 2009, vol. 22, pp. 8–14.
14. S.-M. Cho, B.G. Thomas, and S.-H. Kim: *Metall. Mater. Trans. B*, 2016, vol. 47B, pp. 3080–98.
15. S. Kunstreich, P. H. Dauby, S.-K. Baek, and S.-M. Lee: *Proc. of 5th European Continuous Casting Conf.*, Nice, France, 2005, pp. 37–44.
16. P.H. Dauby: *Rev. Metall.*, 2012, vol. 109, pp. 113–36.
17. K. Jin, S.P. Vanka, and B.G. Thomas: *Metall. Mater. Trans. B*, 2017, vol. 48B, pp. 162–78.
18. H. Bai and B.G. Thomas: *Metall. Mater. Trans. B*, 2001, vol. 32B, pp. 269–84.
19. Z. Liu, B. Li, M. Jiang, and F. Tsukihashi: *ISIJ Int.*, 2013, vol. 53, pp. 484–92.
20. Z. Liu, F. Qi, B. Li, and S.C.P. Cheng: *Int. J. Multiphase. Flow*, 2016, vol. 79, pp. 190–201.
21. K. Cukierski and B.G. Thomas: *Metall. Mater. Trans. B*, 2008, vol. 39B, pp. 94–107.
22. Y. Wang, A. Dong, and L. Zhang: *Steel Res. Int.*, 2011, vol. 82, pp. 428–39.
23. R. Singh, B.G. Thomas, and S.P. Vanka: *Metall. Mater. Trans. B*, 2014, vol. 45B, pp. 1098–1115.
24. B.G. Thomas, L.J. Mika, and F.M. Najjar: *Metall. Mater. Trans B*, 1990, vol. 21B, pp. 387–400.

25. F.M. Najjar, B.G. Thomas, and D.E. Hershey: *Metall. Mater. Trans B*, 1995, vol. 26B, pp. 749–65.
26. S.-M. Cho, B.G. Thomas, H.-J. Lee, and S.-H. Kim: *Iron Steel Technol.*, 2017, vol. 14, pp. 76–84.
27. I. Calderon-Ramos, R.D. Morales, and M. Salazar-Campoy: *Steel Res. Int.*, 2015, vol. 86, pp. 1610–21.
28. M.M. Salazar-Campoy, R.D. Morales, A. Nájera-Bastida, I. Calderón-Ramos, V. Cedillo-Hernández, and J.C. Delgado-Pureco: *Metall. Mater. Trans. B*, 2018, vol. 49B, pp. 812–30.
29. R. Chaudhary, G.-G. Lee, B.G. Thomas, and S.-H. Kim: *Metall. Mater. Trans B*, 2008, vol. 39B, pp. 870–84.
30. C.A. Real-Ramirez, R. Miranda-Tello, L. Hoyos-Reyes, M. Reyes, and J.I. Gonzalez-Trejo: *Indian J. Eng Mater. Sci.*, 2012, vol. 19, pp. 179–88.
31. Q. Yuan: Ph. D. Thesis, University of Illinois at Urbana-Champaign, 2004.
32. Q. Yuan, B.G. Thomas, and S.P. Vanka: *Metall. Mater. Trans. B*, 2004, vol. 35B, pp. 685–702.
33. R. Liu: Ph. D. Thesis, University of Illinois at Urbana-Champaign, 2015.
34. ANSYS FLUENT 14.5-Theory Guide, ANSYS. Inc., Canonsburg, PA, USA, 2012.
35. F. Nicoud and F. Ducros: *Flow Turb. Comb.*, 1999, vol. 63, pp. 183–200.
36. A.W. Cramb and I. Jimbo: *Iron Steelmak.*, 1989, vol. 16, pp. 43–55.
37. J. Lee and K. Morita: *ISIJ Int.*, 2002, vol. 42, pp. 588–94.
38. B.J. Keene: *Int. Mater. Rev.*, 1993, vol. 38, pp. 157–92.
39. A. Kasama, A. McLean, W.A. Miller, Z. Morita, and M.J. Ward: *Can. Metall. Q.*, 1983, vol. 22, pp. 9–17.
40. K.C. Mill and Y.C. Su: *Int. Mater. Rev.*, 2006, vol. 51, pp. 329–351.
41. H. Shin: Ph.D. Thesis, POSTECH, 2006.
42. B. Zhao, S.P. Vanka, and B.G. Thomas: *Int. J. Heat Fluid Flow*, 2005, vol. 26, pp. 105–18.
43. R.M. McDavid and B.G. Thomas: *Metall. Mater. Trans. B*, 1996, vol. 27B, pp. 672–85.
44. B. Xie, J. Wu, and Y. Gan: Proc. of Steelmaking Conference, ISS-AIME, Warrendale, PA, USA, 1991, pp. 647–651.
45. R. Liu, J. Sengupta, D. Crosbie, S. Chung, M. Trinh, and B. G. Thomas: *Proc. of TMS 2011*, TMS, Warrendale, PA, USA, 2011, pp. 51–58.
46. H. Bai and B.G. Thomas: *Metall. Mater. Trans. B*, 2001, vol. 32B, pp. 253–67.
47. Q. Yuan, S. Sivaramakrishnan, S.P. Vanka, and B.G. Thomas: *Metall. Mater. Trans. B*, 2004, vol. 35B, pp. 967–82.
48. J. M. Harman and A. W. Cramb: *Proc. 79th Steelmaking Conf.*, The Iron and Steel Society, Warrendale, PA, USA, 1996, pp. 773–84.
49. H.L.F. Von Helmholtz: *Monatsb. K. Preuss. Akad. Wiss. Berlin*, 1868, vol. 23, pp. 215–28.
50. W. Thomson: *Philos. Mag.*, 1871, vol. 42 (281), pp. 362–377.
51. T. Funada and D.D. Joseph: *J. Fluid*, 2001, vol. 445, pp. 263–83.
52. G.-G. Lee, B.G. Thomas, S.-H. Kim, H.-J. Shin, S.-K. Baek, C.-H. Choi, D.-S. Kim, and S.-J. Yu: *Acta Mater.*, 2007, vol. 55, pp. 6705–12.
53. L. Zhang and Brian G. Thomas: Proc. Of *XXIV National Steelmaking Symposium*, Morelia, Mich, Mexico, 2003, pp. 138–183.
54. H-J Shin, B . G. Thomas, G-G. Lee, J-M. Park, C-H. Lee, and S-H. Kim: *Proc. Materials Science and Technology (MS&T)*, Assoc. Iron Steel Technology, Warrendale, PA, USA, 2004, vol. II, pp. 11–26.
55. ASM. Jonayat and B. G. Thomas: *Metall. Mater. Trans. B*, 2014, vol. 45B, pp. 1842–64.
56. B.E. Launder and D.B. Spalding: *Lectures in Mathematical Models of Turbulence*, Academic Press, London, England, 1972.
57. S.-M. Cho, S.-H. Kim, and B.G. Thomas: *ISIJ Int.*, 2014, vol. 54, pp. 845–54.
58. R. Chaudhary, C. Ji, B.G. Thomas, and S.P. Vanka: *Metall. Mater. Trans. B*, 2011, vol. 42B, pp. 987–1007.
59. S.-M. Cho, S.-H. Kim, and B.G. Thomas: *ISIJ Int.*, 2014, vol. 54, pp. 855–64.
60. R. Chaudhary, B. T. Rietow, and B. G. Thomas: Proc. *Materials Science and Technology (MS&T)*, AIST/TMS, Pittsburgh, PA, 2009, pp. 1090–1101.
61. X. Jin, D. Chen, X. Xie, J. Shen, and M. Long: *Steel Res. Int.*, 2013, vol. 84, pp. 31–39.